

Research Signpost
37/661 (2), Fort P.O., Trivandrum-695 023, Kerala, India



Beam Injection Based Nanocharacterization of Advanced Materials, 2008: 257-294
ISBN: 978-81-308-0226-8 Editors: G. Salviati, T. Sekiguchi, S. Heun and A. Gustafsson



X-ray photoemission microscopy for nanocharacterization of advanced materials

**Chia-Hao Chen¹, Ruth Klauser^{1,*}, Stefan Heun^{2,#}, Yoshio Watanabe³
and Michael Zharnikov⁴**

¹National Synchrotron Radiation Research Center, 101 Hsin-Ann Road Hsinchu 30076, Taiwan; ²Laboratorio Nazionale TASC INFN-CNR, Area Science Park - Basovizza, 34012 Trieste, Italy; ³JASRI/SPring-8, 1-1-1 Kouto Sayo-cho Sayo-gun Hyogo 679-5198, Japan; ⁴Angewandte Physikalische Chemie, Universität Heidelberg, 69120 Heidelberg, Germany

Abstract

The continuous miniaturization and increasing complexity of the materials used in modern technology requires an access to the chemical composition and electronic structure, and a possibility to monitor variations or fluctuations in these properties at sub-micron and nanometer scales. In principle, X-ray photoelectron spectroscopy (XPS) can provide this

Present address: ^{*}CTIX Group, Department of Applied Science, University of California at Davis, Livermore CA 94551, USA; [#]NEST CNR-INFN and Scuola Normale Superiore, Via della Faggiola 19, 56126 Pisa, Italy

Correspondence/Reprint request: Dr. Stefan Heun, Laboratorio Nazionale TASC INFN-CNR, Area Science Park - Basovizza, 34012 Trieste, Italy. E-mail: stefan.heun@sns.it

information. However, in a traditional experimental setup, the spectroscopic signal is obtained from a spot of some 100 μm to millimeters in diameter, and therefore averages over this area. This has led to a strong demand to perform XPS from areas as small as the smallest building blocks of the nanostructures under study, and motivated the development of special instruments which combine spectroscopy and microscopy and allow to perform XPS with the highest possible lateral resolution, namely the direct imaging and the scanning type photoemission microscopes. The first part of this paper reviews the present state and future developments in the field of direct imaging photoemission microscopes, in particular, the use of photoemission electron microscopes (PEEM) in combination with synchrotron radiation. The role of energy filtering and aberration correction is discussed in detail. The second part of the article reviews the state-of-the-art in scanning photoemission microscopy (SPEM). Finally, selected results obtained with PEEM and SPEM on self-assembled monolayers and carbon nanotubes demonstrate the power of these methods.

Introduction

After almost a century of development since the discovery of the photoelectric effect, photoelectron spectroscopy (PES) has become a standard analytical tool in surface and material science providing elemental analysis of surface species and their chemical states [1]. However, not until the late 1980's, an important aspect in PES, namely the lateral resolution, has been seriously considered. Almost all analytical technique can benefit from lateral resolution [2]. PES automatically reaches high spatial resolution in the direction perpendicular to the surface because of the short mean-free-path of the excited photoelectrons. On the other hand, a conventional PES spectrometer, averaging over an area of the order of square millimeters, usually lacks lateral resolution. The main limiting factor for the development of PE microscopy was a relatively low intensity of the emitted photoelectrons per surface area at their excitation with a conventional X-ray source [3]. However, the rapid development of third generation soft X-ray synchrotron radiation light sources around the world, such as, e. g., ALS in Berkeley, USA [4], ELETTRA in Trieste, Italy [5, 6], NSRRC in Hsinchu, Taiwan [7–9], MAX-LAB in Lund, Sweden [10], BESSY II in Berlin, Germany [11], and PLS in Pohang, Korea [12], has allowed to overcome the photon flux limitation, and different types of photoemission microscopy stations have been developed. The main characteristic of these machines is the source brightness provided by insertion devices, either wigglers or undulators, which can deliver a photon beam of high brilliance, which is by several orders of magnitude more intense than that provided by the best conventional X-ray sources.

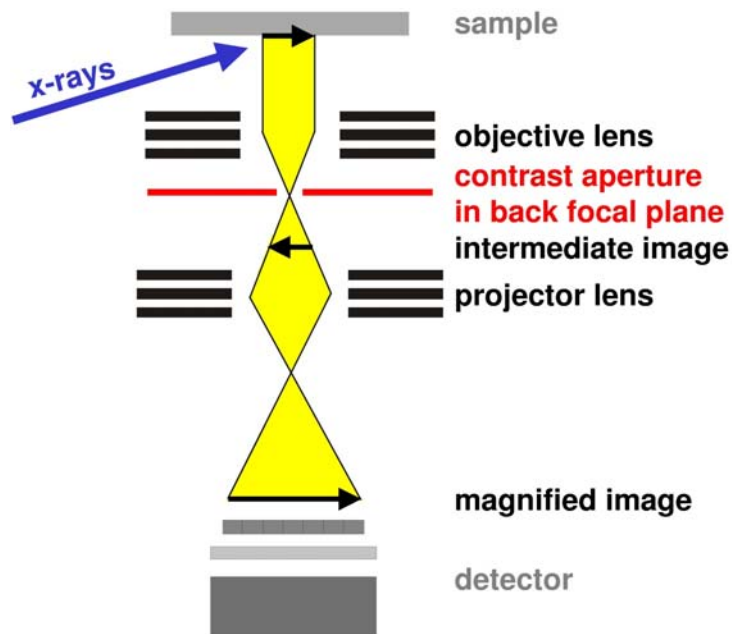


Figure 1. A schematic drawing of a PEEM. The sample is illuminated by monochromatic X-rays. The lateral photoelectron distribution is collected by the objective lens and transferred by a lens system to the detector.

More than 10 years ago, two basic, complementary design principles have been identified for photoemission microscopes [13]: the scanning and the direct imaging type instruments. In the scanning type instruments the photon beam is focused by an optical system (like a Fresnel zone plate or a Schwarzschild objective) on a small spot on the sample. The photoelectrons excited from this area are then collected by a detector. The lateral resolution of the instrument is given by the size of the illuminated area. A surface map can be obtained by scanning the sample relative to the beam.

On the other hand, in the direct imaging type instruments, the sample is illuminated in a larger area and the photoelectron yield image is magnified by an electron optical system. The most popular instrument of this type is the photoemission electron microscope (PEEM) which will be discussed in the following.

Imaging photoemission microscopy

A PEEM employs electrostatic or magnetic lenses to form a magnified image of the local photoelectron yield of the sample on a screen [14]. Typical fields of view of the microscope range from $1\ \mu\text{m}$ to $100\ \mu\text{m}$. To excite the photoelectrons, the sample is homogeneously illuminated by monochromatic X-rays in a spot the size of which ideally matches the field of view of the microscope. A PEEM allows continuous imaging with video rate [15]. No

sample scanning is necessary. A basic PEEM is shown in Figure 1. The photoelectrons emitted from the sample are accelerated by a high electric field between the sample and the objective lens. The image produced by the objective lens is magnified by the projector lens onto a detector. High fields at the sample are generally needed for collection efficiency and lateral resolution. Therefore samples with sharp tips cannot be studied since field emission starts at fields well below those used for imaging.

A PEEM can be equipped with an electron gun and operated as a low energy electron microscope (LEEM) [16]. The separation between incoming and outgoing electrons is achieved by a magnetic prism (sector field). The electrons emitted or reflected from the surface are transferred into the image plane of the microscope, where a magnified image of the sample can be observed with a video camera or a CCD camera. A LEEM can be used to obtain real space images of the sample with a lateral resolution of 7-8 nm [17, 18], or to measure the intensity distribution in reciprocal space (low energy electron diffraction (LEED)). The LEED pattern can be obtained from a sub-micrometer-sized spot on the sample. A photograph of a commercial LEEM system is shown in Figure 2.

The lateral resolution of a PEEM/LEEM is determined by three quantities: (a) spherical aberrations, (b) chromatic aberrations, and (c) diffraction [11]. Spherical aberrations can be reduced by cutting the electrons which pass the lenses far from the center, i. e., by reducing the angular acceptance of the microscope. For this purpose, a contrast aperture is usually placed in the back focal plane (or an equivalent plane) of the PEEM. Furthermore, due to the chromatic aberrations, a focal point of the microscope is smeared out along the

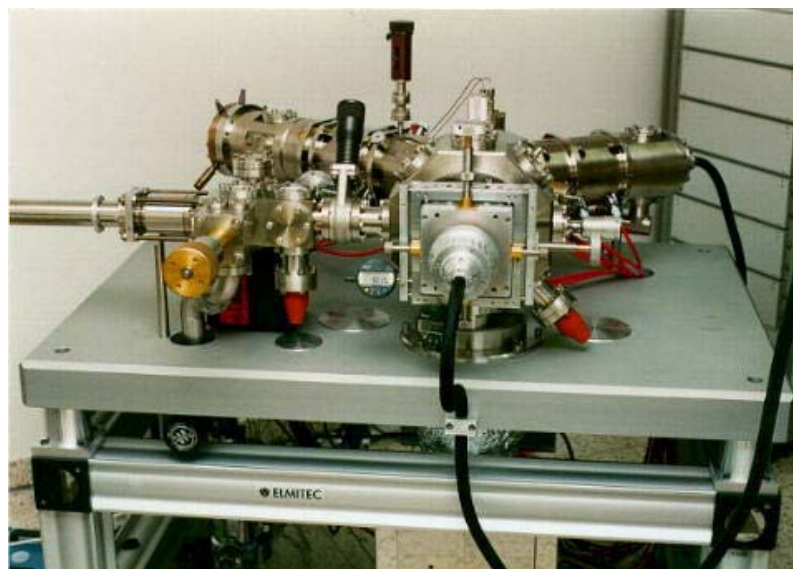


Figure 2. Photograph of a LEEM instrument. Courtesy of Elmitec company.

optical axis. Only electrons with the proper energy are focused into the aperture, which reduces the width of the energy distribution of the electrons transmitted through the PEEM [19, 20]. Therefore the use of a contrast aperture reduces the aberrations of the microscope, at the expense of transmission. Reducing the diameter of the contrast aperture, the lateral resolution of the microscope can be improved, until finally diffraction at the aperture becomes the dominating effect, and further reduction of the aperture diameter reduces the transmission of the microscope without further improvement in lateral resolution. With X-ray illumination, a standard PEEM like the PEEM2 at the ALS can reach a lateral resolution of 20 nm [20].

A photoelectron spectrum obtained with X-rays consists of three parts [21]: the secondaries peak at low kinetic energy ($\approx 0 - 20$ eV), the core level and Auger peaks at energies characteristic for the elements and their chemical state, and the valence band or Fermi edge at the high kinetic energy cutoff. The width of the spectrum (i. e., the difference between high and low energy cutoff) equals the photon energy minus the work function of the sample, and in synchrotron radiation experiments can therefore be several ten to hundred eV large. However, lowering the photon energy to the UV, the valence band moves closer to the secondaries peak, and the photoelectrons' energy distribution curve gets narrower, thereby reducing the effect of chromatic aberrations. Under such conditions a lateral resolution of up to 7 nm has been achieved with PEEM [22, 23].

The early PEEM work has been performed with deuterium or mercury lamps [24]. In these experiments, lateral variations of the work function of the sample were used as contrast mechanism. However, to do real elemental sensitive work, higher photon energies are necessary to excite atomic core levels. Therefore spectroscopic work with PEEM is usually done at a synchrotron. Most of this work has utilized soft X-rays and ultraviolet photons (10 – 2000 eV) in order to achieve high surface sensitivity. However, there are first attempts to use PEEM also in combination with hard X-rays which allows to image buried interfaces [25, 26]. Alternatively, the use of PEEM in transmission mode makes PEEM a bulk sensitive probe [27–31]. Basically, in this mode of operation, the variation in the X-ray intensity due to the absorption contrast of the sample is converted into secondary electrons which are detected by the PEEM system.

Spectroscopy with a PEEM can be performed by scanning the photon energy and measurement of the optical absorption edge of elements of interest. This technique is called μ -XANES (X-ray absorption near edge spectroscopy). It allows to perform spectroscopy with the lateral resolution of the PEEM. It works because the total photoelectron yield is approximately proportional to the photoabsorption coefficient [32]. Therefore, secondary electrons are used

for imaging [19, 33]. A requirement for this kind of experiments is a tunable X-ray source, which is naturally given in a synchrotron.

Even with sufficiently high photon energies, a basic PEEM (as described above) cannot be used for X-ray photoelectron spectroscopy (XPS) because it is not equipped with a photoelectron energy analyzer. Therefore, in order to perform photoelectron spectroscopy with a PEEM, the system has to be equipped with an energy filter. The advantages of such a combination were discussed in detail by Bauer [34]. However, the implementation of an energy filter in a PEEM is not only useful to obtain energy filtered images and to collect photoemission spectra. It also allows to reduce chromatic aberrations. Therefore, even for μ -XANES experiments, the use of an energy analyzer is beneficial: it allows to select a narrow energy window around the maximum of the secondary electron energy distribution and to improve the lateral resolution of the microscope without unacceptable loss of intensity.

Two principal ways lead to an energy analysis of the photoelectrons with lateral resolution. One possibility is to perform area selective spectroscopy: an aperture is used to select an interesting region within the field of view of the microscope. Photoelectrons from other parts of the sample are blocked, and only the photoelectrons from the interesting region can reach the analyzer. Therefore, the PEEM acts as a high-performance transfer lens for the analyzer. The diameter of the analyzed region can be as small as 1 μm . A commercial energy analyzer (hemispherical [35] or cylindrical [36]) can be used for this purpose, which allows to rely on tested standard equipment. An energy resolution of 190 meV has been demonstrated with such setup [37].

The second possibility is to filter the whole PEEM image energetically. Several methods have been proposed to achieve this goal. In a simple setup, a mesh is inserted in the PEEM. If the mesh is biased, only photoelectrons with a kinetic energy higher than the bias can pass the mesh which therefore acts as a high-pass filter. By taking two images at slightly different bias and calculating their difference, energy-filtered images can be reconstructed (*spectromicroscopy*). By increasing the bias of the mesh, more and more photoelectrons are cut out, and the energy spread in the image is reduced. By differentiation, the energy distribution curve of the photoelectrons from the sample can be obtained from an area as small as 1 μm (*microspectroscopy*). An energy resolution of about 1 eV is reported for this setup with synchrotron and laboratory X-ray sources [38].

In a more sophisticated setup, the whole PEEM image is energy filtered by a band-pass filter, i.e., only electrons with a certain energy $E_0 \pm \Delta E$ can contribute to the image. Different solutions have been proposed and realized.

In a time-of-flight (TOF) analyzer, photoelectrons excited by a pulsed light source are dispersed by the time T they need to pass a drift tube of length L with a velocity $v = L/T$. The dispersion is given by dT/dE with $E = \frac{m}{2}v^2$

(m : electron mass). For $L = 30$ cm we obtain a variation of dT/dE from 8 ns/eV at 10 eV to 0.25 ns/eV at 100 eV. Therefore, the single light pulses should be separated at least by some 10 ns in order to avoid an overlap of spectra from consecutive pulses, which means that measurements with TOF require a synchrotron operated in single- or few-bunch mode. Obviously, this kind of PEEM requires a detector with high temporal resolution, which is the main technical difficulty in this approach. With a delay line detector, a time resolution of 0.5 ns has been achieved [39, 40], which corresponds to a theoretical energy resolution of 60 meV at 10 eV and of 2 eV at 100 eV. In first test experiments, an energy resolution of 400 meV at 43 eV has been demonstrated [40], while a lateral resolution of less than 100 nm has been reported [39]. In the future, PEEM systems with TOF analyzer might become very useful in combination with pulsed X-ray laser sources.

A Wien filter uses an electric and magnetic field which are perpendicular to each other so that only electrons with a particular energy can pass the filter without deflection [41–43]. Although an energy resolution of 0.1 eV has been calculated for this design, only 1 eV has been demonstrated so far, mainly because at higher resolution the intensity would be unacceptably low [44].

An Omega filter consists of four sector magnets arranged like the greek capital letter Omega. It is used in the SMART microscope at BESSY-II [45]. An energy resolution of 0.5 eV has been achieved so far [11].

The analyzer type most commonly used in photoelectron spectroscopy is the electrostatic spherical energy analyzer. Such analyzers were also combined with PEEM. Systems with 90° analyzer [46] and 180° analyzer [17, 47] have been build and successfully operated. A combination of two 90° analyzers has been proposed [48, 49], as has a system of two opposite concentric spherical deflectors connected by a relay lens [50, 51]. Recently a double hemispherical 180° analyzer has been built and connected to a PEEM (NanoESCA) [52–54]. The NanoESCA provides a high transmission even at high photoelectron kinetic energies and is therefore particularly suited for use with laboratory X-ray sources (Mg K_α and Al K_α). Electrostatic spherical analyzers in connection with PEEM have demonstrated an energy resolution of 100 meV [52].

Most of the results in photoelectron spectroscopy using a PEEM published so far have been obtained with electrostatic hemispherical analyzers. A schematic drawing of such an instrument is shown in Figure 3. It is a commercial LEEM system with energy filter [55], based on a design by Veneklasen and Bauer [46, 56], and has been named spectroscopic photoemission and low energy electron microscope (SPELEEM). Such instruments are operational in Elettra [17], the Swiss Light Source [57], and SPring-8 [58], and several other synchrotron light sources are preparing to install a SPELEEM, as well. The SPELEEM is a LEEM/PEEM with full spectromicroscopic capabilities. Besides LEEM and LEED, the use of an electron

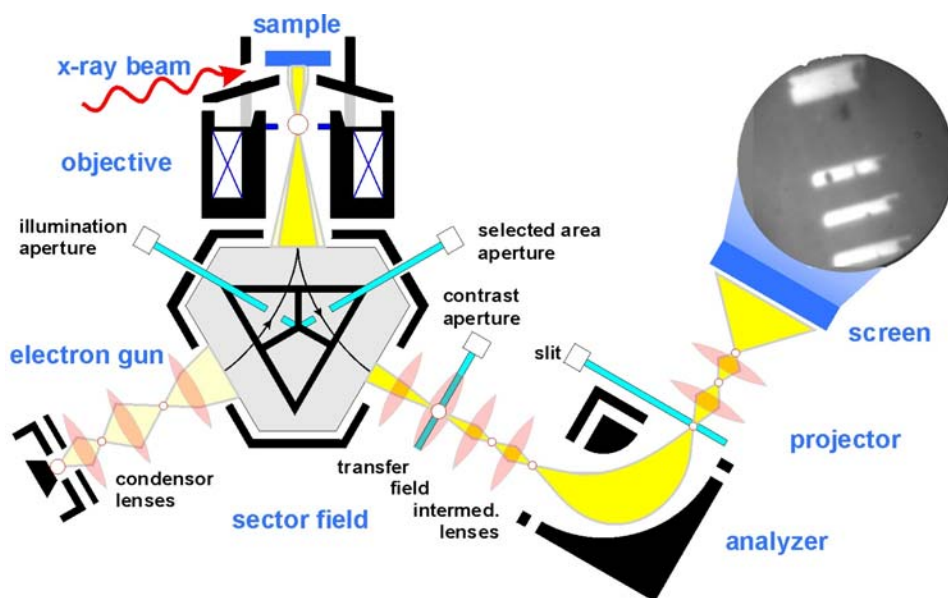


Figure 3. Schematic drawing of the SPELEEM instrument.

gun and an energy analyzer allows measurement of the energy distribution of the electrons (electron energy loss spectroscopy (EELS)) from a micrometer spot on the sample. In complete analogy to this, three modes of operation are available when working with photons: Imaging PEEM (*spectromicroscopy*), dispersive plane imaging (*microspectroscopy*), and diffraction mode (photoelectron diffraction (PED)) [17, 59].

In the imaging PEEM mode, the photoelectrons from the sample are collected, selected in energy, and projected on a phosphorous screen where a magnified image of the sample surface is displayed and recorded by a CCD camera. The best lateral and energy resolution are 22 nm and 250 meV, respectively [17, 60]. In each image the intensity represents the photoelectron yield at a fixed kinetic energy relative to that specific location. For each pixel it is possible to plot the intensity as a function of energy, thereby obtaining local photoemission spectra. The images are isochromatic within 0.1 eV, i.e., within 0.1 eV each pixel of the image corresponds to the same energy [60].

In dispersive plane imaging, all the photoelectrons originating from a micrometric region of the sample are collected and dispersed in energy by the hemispherical analyzer. Electrons with different energies are then projected on different regions of the phosphorous screen along a line. The intensity along the projected line corresponds to the photoemission spectrum. A best energy resolution of 150 meV has been achieved in this mode [60]. The dispersive plane mode, although at the expense of lateral resolution, has the advantage of faster acquisition times (of the order of seconds for a complete spectrum) which allows a fast time-resolved analysis.

In the last years, energy-filtered PEEM has been the method of choice for the investigation of several material systems of current research interest, like semiconductor quantum dots [61–63], magnetic materials [64], oxide nanostructures [65–67], catalysis and surface reactivity [60, 68], surface science [54], carbon nanotubes [69], and self-organization processes at surfaces [70].

While all methods to improve the lateral resolution of the PEEM discussed so far did not eliminate the aberrations of the lenses but reduced their influence at the expense of transmission of the microscope, the ideal solution would be to build an optical system without aberrations. However, in contrast to light optics in the visible where aberrations can be corrected by a lens combination (achromat), Scherzer demonstrated already in 1936 that all conventional electron lenses have aberrations of the same sign, and therefore it would be impossible to construct an electron–optical achromat with conventional electron lenses.

Several methods have been proposed to overcome this limitation and to build aberration corrected electron microscopes. The moving focus method improves the lateral resolution of the electron microscope by a superposition of images taken at different focus values [71]. The time-of-flight technique reduces chromatic aberrations with a fast switching lens field [72]. Electrons with different energies (which give rise to chromatic aberrations) have different velocities and pass therefore the corrector at different times. If the corrector is fast enough, it can change the focal properties of the lens so that all energies are focused in the same point. A correction of spherical aberrations with this approach, however, seems much more complex. Multipole lenses are already successfully employed in scanning and transmission electron microscopes [73, 74], and sub-Å resolution has been demonstrated [75]. A similar approach, using a multipole Wien filter, is now under development for PEEM [76, 77]. Finally, the use of an electron mirror has been proposed for aberration correction in PEEM and LEEM [78]. While all conventional electron lenses have aberrations of the same sign, an electron mirror (like the multipole lenses) produces aberrations of the opposite sign and allows therefore to compensate for the aberrations of the lenses.

A new generation of aberration–corrected PEEMs is now under construction: the SMART project at BESSY–II [11, 79] and the PEEM3 project at the ALS [80–84]. These instruments will use an electron mirror for aberration correction. For the SMART microscope, a best lateral resolution of 0.5 nm has been calculated. Alternatively, at a lateral resolution of 10 nm the calculated transmission of the SMART will be 3000 times higher than that of an uncorrected PEEM with the same resolution [45]. For the PEEM3, the highest resolution predicted is 5 nm at 2% transmission, while a transmission of $\approx 30\%$ has been calculated at a resolution of 20 nm. This has to be compared to a transmission of 1% for the uncorrected PEEM2 at its resolution limit of 20 nm [81, 83].

Scanning photoemission microscopy

The direct imaging type of X-ray photoemission microscopes has been described in the previous section; in the following the scanning photoelectron microscope (SPEM) will be introduced.

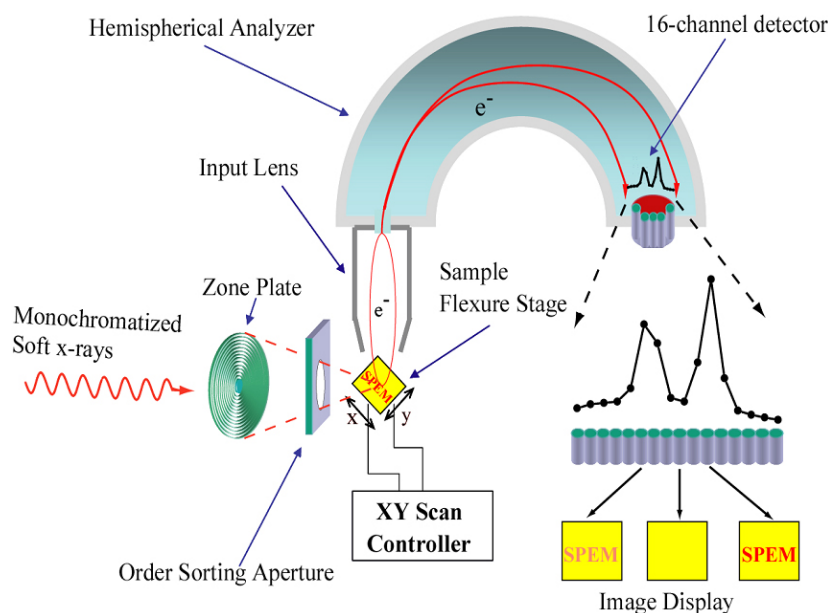


Figure 4. The major components of a zone-plate-based SPEM system. The combination of a zone plate and an order sorting aperture forms the focusing optics. The sample scanning system and electron energy analyzer are two other key components.

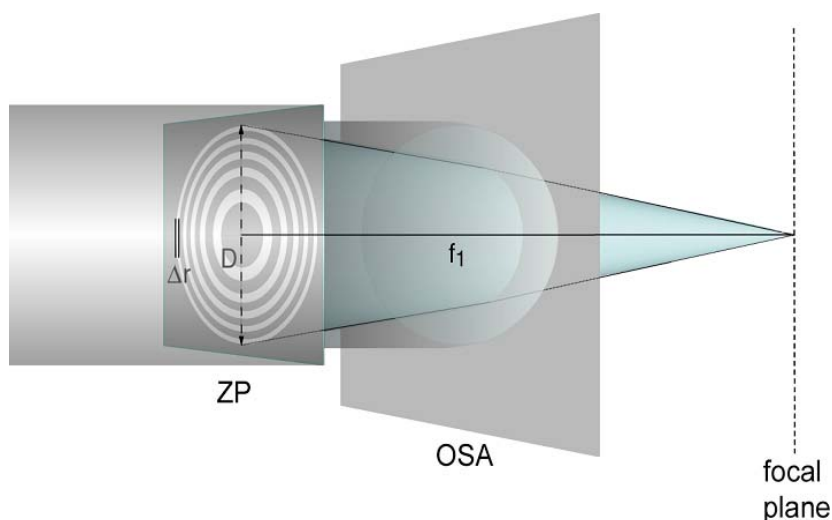


Figure 5. A schematic drawing of a Fresnel zone plate (ZP) and an order sorting aperture (OSA). The zone plate has a diameter D , an outermost zone width Δr , and a focal length of f_1 . Shown in the figure are only the non-diffracted and the first order diffraction beam.

SPEM instruments employ photon optics such as Fresnel zone plate (ZP), Kirkpatrick-Baez (KB) mirror, or Schwarzschild objective to focus the incoming light, mostly in the energy range of ultraviolet (UV) and soft X-ray. By raster-scanning the sample with respect to the focused photon beam and collecting the photoelectrons emitted from the illuminated micro-spot, a two dimensional distribution of photoemission intensity can be constructed. The three major components of the SPEM system are (1) focusing optics, (2) electron energy analyzer, and (3) sample scanning mechanism [7, 8], as illustrated in Figure 4.

The focusing optics

Among the focusing optics that can be applied in the UV and X-ray range, the ZP offers the best compromise between spatial resolution, delivered photon flux, and energy tunability [85]. We will therefore concentrate our report on ZP-based SPEM.

A Fresnel zone plate is a circular diffraction grating with a radially increasing line density that acts as a lens for short wavelength radiation. A typical ZP consists of alternating transparent and opaque rings whose width decreases as the diameter increases, as illustrated in Figure 5. The transparent zones are arranged in such a way that the optical path difference through the sequential zones are exactly one wavelength, and therefore light coming through these zones undergoes a positive interference at the focal points [86, 87]. Like any diffraction grating, ZP has an infinite number of the diffraction orders, with the focal length f_m in the m th order, expressed as [86, 87]:

$$f_m = \frac{D\Delta r}{m\lambda} \quad (1)$$

where D is the ZP diameter, Δr is the outermost zone width of the zone plate lens, and λ the wavelength of X-rays. In order to filter out all unwanted diffraction orders, an order sorting aperture (OSA) has to be inserted between the ZP and focal plane [87]. The geometrical arrangement of ZP and OSA is shown in Figure 5.

By applying the Rayleigh criterion, the diffraction limited spatial resolution δR_m in the m th diffraction order of a perfect lens will be [86]:

$$\delta R_m = \frac{1.22\Delta r}{m} \quad (2)$$

However, in a real system, the spatial resolution of the m th diffraction order ($\delta R_{m,r}$) is a function of the diffraction-limited resolution δR_m , the light monochromaticity $\delta_c = D\Delta E/E$ at photon energy E , and the demagnified source size $\delta_{d,m}$, which is equal to the source size δ_s times f_m divided by the source to ZP distance L [88].

$$\begin{aligned}\delta R_{m,r} &= \sqrt{(\delta R_m)^2 + (\delta_c)^2 + (\delta_{d,m})^2} \\ &= \sqrt{\left(\frac{1.22\Delta r}{m}\right)^2 + \left(D\frac{\Delta E}{E}\right)^2 + \left(\frac{\delta_s f_m}{L}\right)^2}\end{aligned}\quad (3)$$

Most of the ZP-based SPEM stations are located at synchrotron radiation light sources. The typical energy resolving power of soft X-ray beamlines is in the range of several thousands, and the source to ZP distance is at least several meters. According to Eq. (3), the diffraction-limited spatial resolution given by Eq. (2) is therefore still a good approximation.

As mentioned above, the focal length of a ZP depends on the photon energy, outermost zone width, and the diameter of the ZP. For a ZP of 200 μm diameter and 100 nm outermost zone width, the focal length will be 4–13 mm for a photon energy ranging from 250 to 800 eV. The OSA, however, is only about a quarter of the focal length away from the sample, which can be 1 mm or even less for smaller-sized ZPs. Consequently, the precise positioning of the ZP and OSA is essential for the optimum performance of a SPEM system. A practical way is to mount the ZP and OSA on piezoelectric-driven crossroller-slide stages, which can move ZP and OSA both separately and together through their common base plate [7–9]. If ZP and OSA are perfectly aligned, a symmetric doughnut-shaped pattern can be observed on a phosphor screen behind the sample

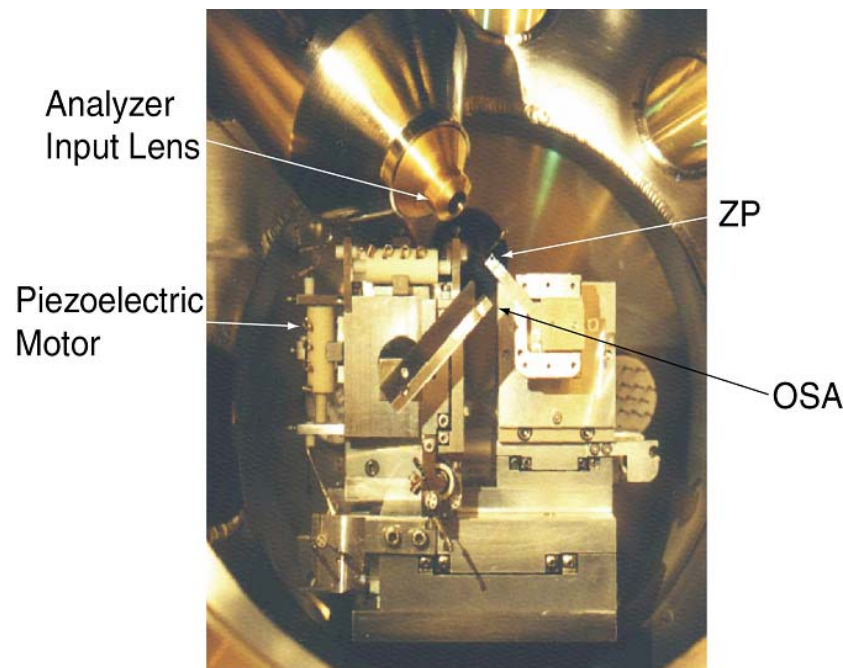


Figure 6. A photo taken from inside the SPEM chamber, showing the analyzer input lens, focusing optics, and the alignment mechanism of the optics. Note that the sample stage has been removed to make the optics visible.

stage. Figure 6 shows the ZP and OSA positioning mechanism used at the NSRRC-SPEM station.

One of the disadvantages of the ZP-based SPEM system is its dependence of the focal length on the photon energy. When the photon energy is lowered, the OSA needs to be placed closer to the sample, which can shade the emitted photoelectrons. For applications involving a low photon energy but requiring a high lateral resolution, like spatially resolved UPS, Schwarzschild optics will, therefore, be a better choice [6, 89, 90].

Another disadvantage of ZP optics is its low diffraction efficiency. The efficiency of a standard Au amplitude ZP in the first order diffraction is about 10% [91]. By replacing the opaque zones with transparent but phase-shifting ones, the efficiency can be enhanced to about 20% [92]. Note that the spatial resolution of a ZP can be improved by using higher diffraction orders as shown by Eq. (2). However, the respective photoelectron signal will be, regrettably, too low for imaging, since the diffraction efficiency is inverse proportional to m^2 [85].

The electron energy analyzer

In the pioneering age of the SPEM development, the analyzer mostly used was the cylindrical mirror analyzer (CMA) [93, 94]. However, due to the poor energy resolution and the low analyzer acceptance [95], the analyzers employed in most SPEM systems nowadays are hemispherical sector analyzers (HSA) with a multi-channel detector (MCD). Since the photoelectrons are energy dispersed in the exit plane of the HSA, the use of a MCD allows a simultaneous collection of photoelectrons of different kinetic energies. The respective signals can be used for image formation. For example, the SPEM at NSRRC has a 16-channel detector that allows a simultaneous acquisition of a set of 16 images corresponding to different kinetic energies of photoelectrons in a single scan [7–9]. The images can be further processed, including summing of all channels and the selection and subtraction of the individual channels, necessary, for example, for background correction.

The sample scanning mechanism

Generally, it is easier to move the sample than the focusing optics. Therefore, most of the synchrotron-based SPEM stations utilize the synchronized scanning of the sample relative to the focused photon beam provided by the optics.

In order to scan the sample surface in both millimeter and micrometer length range, SPEM stations are usually equipped with two sets of sample positioning and scanning mechanisms, viz., a mechanical step motor for long range x-y-z motion and coarse scanning, and an ultrahigh vacuum (UHV)-compatible piezoelectric stage for precise x-y positioning and scanning [3, 7]. Both scanning mechanisms are operated under computer control and are synchronized with the data acquisition.

SPEM can operate in either imaging (spectromicroscopy) or microspectroscopy mode. In the imaging mode, the sample is raster scanned with respect to the photon beam, and the photoelectrons emitted from the beam spot are synchronously collected. Each pixel of the image corresponds to the intensity of the photoelectron signal at a particular place on the sample surface. The image represents then the distribution of the photoelectron yield related to a specific chemical element, which is a measure for its local concentration. In addition, binding energy shifts can be used for mapping chemical states of each element on the sample surface.

With the multi-channel detection capability, images of several different chemical states can be obtained in one scan, which can reduce the acquisition time drastically. An example of the chemical state mapping taken with a 16-channel MCD is given in Figure 7. The sample is a silicon-based IC chip with patterns

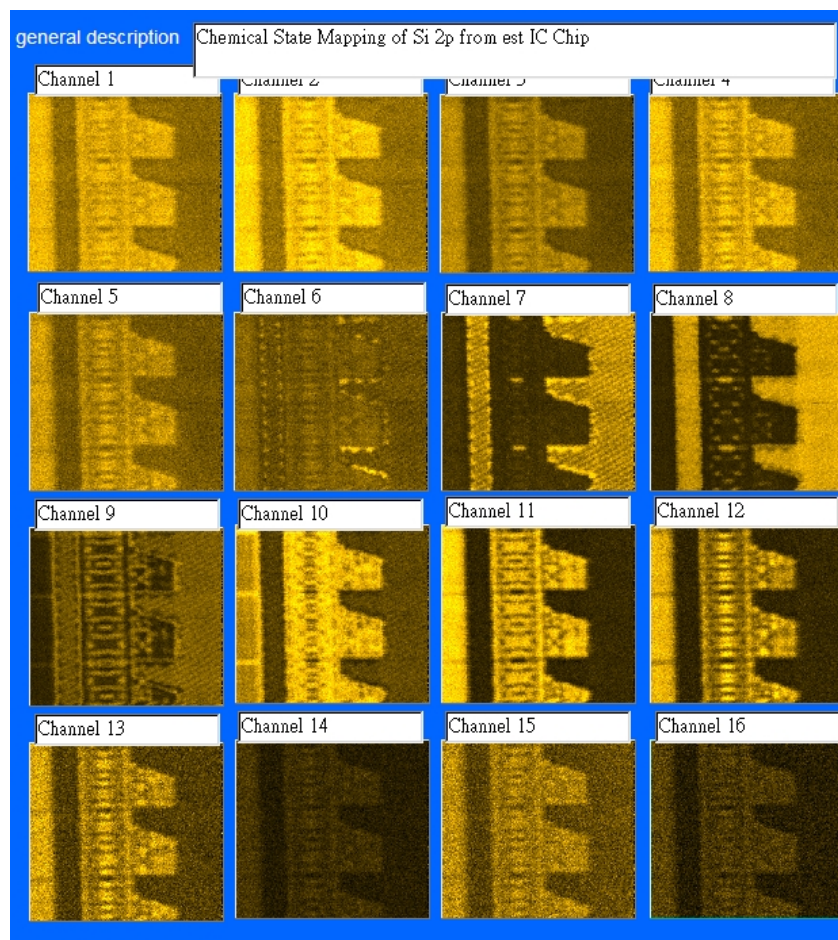


Figure 7. The Si 2p SPEM images of a silicon-based IC chip. The intensity contrast is due to the spatial variation of different chemical states, namely SiO₂, poly-Si, and TiSi₂. The images were taken at a photon energy of 382 eV with an image size of 200 pixel × 200 pixel, a pixel width of 300 nm, a dwell time of 50 ms, and a total acquisition time of about 30 minutes.

of poly-silicon and titanium silicide (TiSi_2) on a silicon substrate with a thin silicon dioxide surface layer. The energy window of the MCD was selected to cover the whole Si 2p range. The images related to the channels number 8, 11, and 12 correspond to the binding energies of silicon in SiO_2 , poly-Si and TiSi_2 , respectively, and represent, thus, the spatial distributions of the respective chemical states.

The second mode of a SPEM system is PE spectroscopy from a small spot area, so-called μ -XPS or μ -UPS. It is a detailed PE spectroscopic analysis of selected areas where the SPEM images show particularly interesting features. μ -XPS spectra from uniform areas can also be taken while keeping the sample scanning [96], which decreases the photon exposure per surface area. This is particularly useful for radiation-sensitive samples, which can degrade fast upon photon illumination.

It should be pointed out that some restrictions exist for the SPEM technique. The samples need to be a conductor or semiconductor. While a flood gun is frequently used for XPS measurements on insulating samples, it is regrettably not applicable for ZP-based SPEM: since the optics is quite close to the sample surface, the electrons delivered by the flood gun cannot easily reach the sample and compensate the charging. Secondly, since the light is focused into a tiny spot, the local photon density is extremely high, which can cause artifacts in the images, as well as radiation-induced damage of the sample [97]. Several ZP-based SPEM systems are presently in operation, e.g., at ELETTRA in Italy, at PLS in Korea, and at NSRRC in Taiwan. The standard spatial resolution of those systems is in the range of 100 nm. A HSA with a 48-channel MCD has been implemented at the ELETTRA-SPEM [85]. A larger number of channels within the energy window defined by the pass energy reduces the energy steps between the images related to the individual channels.

It is important to mention that besides SPEM, there is another scanning type microscope employing ZP as the focusing optics: the scanning transmission X-ray microscope (STXM). STXM detects the intensity distribution of transmitted photons of a particular energy. This technique relies upon X-ray absorption spectroscopy to obtain chemical information [95]. Since it is a photon-in photon-out technique, no UHV is needed, and the range of materials is not only limited to conductors and semiconductors. This makes STXM a quite versatile instrument with easier operation and generally higher spatial resolution, but of course with lack of the surface sensitivity that photoelectron spectroscopy can offer.

With continuous efforts devoted to the improvements of the focusing optics [98, 99] and the development of new synchrotron radiation light sources with higher brightness, the spatial resolution and overall performance of SPEM are expected to improve, and, hopefully, more systems will be built in the near future. However, the demand on new SPEM systems will essentially depend on

the scientific merit. The already existing systems have recently been applied to investigations of the local electronic structure of various semiconductor nanostructures, such as GaN nanowires [100], ZnO nanorods [101, 102], and AlN nanotips [103], and the atomic force microscopy (AFM)-induced formation of silicon carbide nanowires [104]. Other studies included the dynamics of surface chemical processes on catalytic transition metal surfaces [105, 106], the defect formation in organic light-emitting devices [107], and the spatial chemical inhomogeneity of ferromagnetic semiconductors [108]. The above list shows a broad range of scientific and technological areas where SPEM can significantly contribute. Moreover, SPEM is truly a microprobe technique, which offers an additional option of using the focused beam for pattern fabrication. This will be addressed in detail in the first part of the following section.

Application examples

Self-assembled monolayers

The development of novel approaches for the fabrication of structures and patterns on micro- and nanometer length scales attracted a lot of attention in recent years, especially in the field of chemical and biological research. Promising materials for these applications are chemisorbed monomolecular films: self-assembled monolayers (SAMs) [109, 110]. SAMs are well-ordered and densely packed 2D-assemblies of long chain molecules attached to a suitable substrate [111]. The flexible molecular architecture of the SAM constituents allows using a wide range of substrates and provides an easy way to tailor surface properties, such as wetting, lubrication, adhesion, and corrosion. These properties can be controlled by both selection of suitable molecules and the physical modification of the respective SAMs through their exposure to ions, X-ray photons, UV light, or electrons [112]. Such modified monolayers can then be used as templates for the selective attachment of various functional moieties and macromolecules. The adjustable properties and molecular size of their constituents make SAMs an ideal platform for the fabrication of micro- and nanostructures.

Various approaches for the fabrication of micro- and nanopatterns on the SAM basis have been developed during the past two decades, including microcontact printing [113, 114], dip-pen lithography [115, 116], ultraviolet interferometric lithography [117], scanning microprobe printing [118–122], electron beam patterning [123–125], and X-ray lithography using a focused soft X-ray beam from SPEM [126, 127]. Among the above approaches, electron beam patterning is probably most attractive due to a deep understanding of the phenomena occurring upon irradiation of ultrathin organic films with ionizing radiation and the possibility to use well-established setups from conventional electron beam lithography.

The precise adjustment of the properties of a SAM resist relies on the detailed knowledge of the physical and chemical processes upon its irradiation. Such knowledge is predominantly gained by various spectroscopical techniques, such as, e. g., X-ray photoemission spectroscopy, X-ray absorption spectroscopy, mass spectroscopy, and infrared spectroscopy. However, most of these methods lack lateral resolution. For micro-patterned SAMs, these techniques will be unable to offer microscopical or mesoscopical information. On the other hand, the imaging of the SAM-based lithographic patterns was mostly carried out by scanning electron microscopy (SEM) or AFM, offering a high spatial resolution, but lacking chemical information. It was, therefore, desirable to implement an imaging technique based on the chemical identity of the SAM constituents and to perform a direct spectromicroscopical characterization of the patterned SAMs [7, 128]. This has been achieved by SPEM [7, 126, 127] and PEEM [129–131] techniques, as will be demonstrated in the following sections.

SAM-based lithographic patterns by SPEM

The spectroscopic analysis of the complex phenomena occurring at the interactions of electrons or X-rays with SAMs showed that there are two major competitive processes, viz., decomposition/desorption of the film and cross-linking of the neighboring moieties [109]. The former process is the dominant effect for the aliphatic SAMs, whereas quasi-polymerization prevails in the aromatic films, which greatly reduces their damage [132]. Keeping such a film intact, one can modify the functional tail group to create a new chemical identity of the film surface or a surface area [133]. Note that the response of SAMs to low-energy electrons and soft X-rays is similar, since the major impact on SAMs upon X-ray irradiation is provided by photoelectrons and inelastic secondary electrons [134].

SPEM is not only a powerful tool to provide chemical information on the submicrometer length scale, but also an approach to create chemical patterns on the basis of monomolecular resists by the focused soft X-ray beam. The advantages of this approach lie in its high flexibility and applicability to both fabrication and characterization of the monomolecular chemical patterns. With these advantages, *in situ* characterization of the fabricated SAM patterns becomes possible, which makes the chemical analysis more reliable [126, 127], and which is not easy to achieve by other means of the pattern fabrication.

Two different kinds of SAMs were used in this series of studies, namely, the SAMs formed from alkanethiols (AT) and semifluorinated alkanethiols (SFAT). The AT SAM used was hexadecanethiolate or C16 ($\text{CH}_3(\text{CH}_2)_{15}\text{SH}$) while SFAT SAMs were $\text{CF}_3(\text{CF}_2)_9(\text{CH}_2)_2\text{SH}$ (F10H2) and $\text{CF}_3(\text{CF}_2)_9(\text{CH}_2)_{11}\text{SH}$

(F10H11). The substrate and film preparations were performed in accordance with the standard procedure [109, 135]; a detailed description of the synthesis of the SFAT compounds can be found elsewhere [136–139].

The *ex situ* e-beam patterning was carried out in an UHV system by a 300 eV electron beam (an electron dosage of $10000 \mu\text{C}/\text{cm}^2$) through a mask with mesh sizes of #2000 (proximity printing). The resulting patterns were exposed to ambient and inserted into the SPEM chamber for further characterization [126].

The samples for the *in situ* patterning experiments were F10H11 on Au and F10H2 on Ag substrate. The spot size of the focused soft X-rays was about 100 nm. The parameters of the focusing optics were kept the same for both writing and imaging so that the smallest line width for the patterning and the best spatial resolution for the imaging were achieved. The exposure time and step size have been chosen differently to perform a desirable film modification at writing and achieve the best compromise between the image quality and beam damage during the imaging [127].

Electron-beam patterned SAMs

Alkanethiolates on gold substrate are the most studied SAMs and often used as a test system. Figure 8(a) shows the 16-channel μ -XPS Au 4f spectra for a C16/Au pattern, along with the Au 4f_{7/2} image, which corresponds to channel 10 (a higher channel number corresponds to a lower binding energy). The spectra were derived from a stack of 16 successive SPEM images making the intensity summation over 20 pixel \times 20 pixel squares either on the mesh stripes or the square openings, as indicated in the figure by the arrows. Figure 8(b) presents the C 1s image along with the respective 16-point C 1s spectra. The image corresponds to channel number 9.

The Au 4f_{7/2} and C 1s images in Figures 8(a) and 8(b), respectively, exhibit inverse contrast. The Au 4f intensity from the nonirradiated areas (mesh stripes) is higher than that from the irradiated areas (square opening), whereas the inverse intensity relation is observed for the C 1s image.

The contrast observed in the Au 4f_{7/2} and C 1s images is in contradiction with the results of *in situ* spectroscopic measurements, which revealed a reduction of the SAM thickness as a result of irradiation-induced desorption of the SAM constituents and their fragments [109, 140]. The respective thickness reduction depends on the length of the alkyl chain and the electron dosage. In the case of C16/Au, 30% of thickness reduction (with respect to the pristine layer) has been reported for a dose of $10000 \mu\text{C}/\text{cm}^2$ [140, 141]. In accordance with these results, the areas exposed to the electron irradiation of the patterned SAMs should reveal a larger Au 4f and a smaller C 1s signals. On the contrary, the opposite intensity relations are observed in Figure 8. This apparent

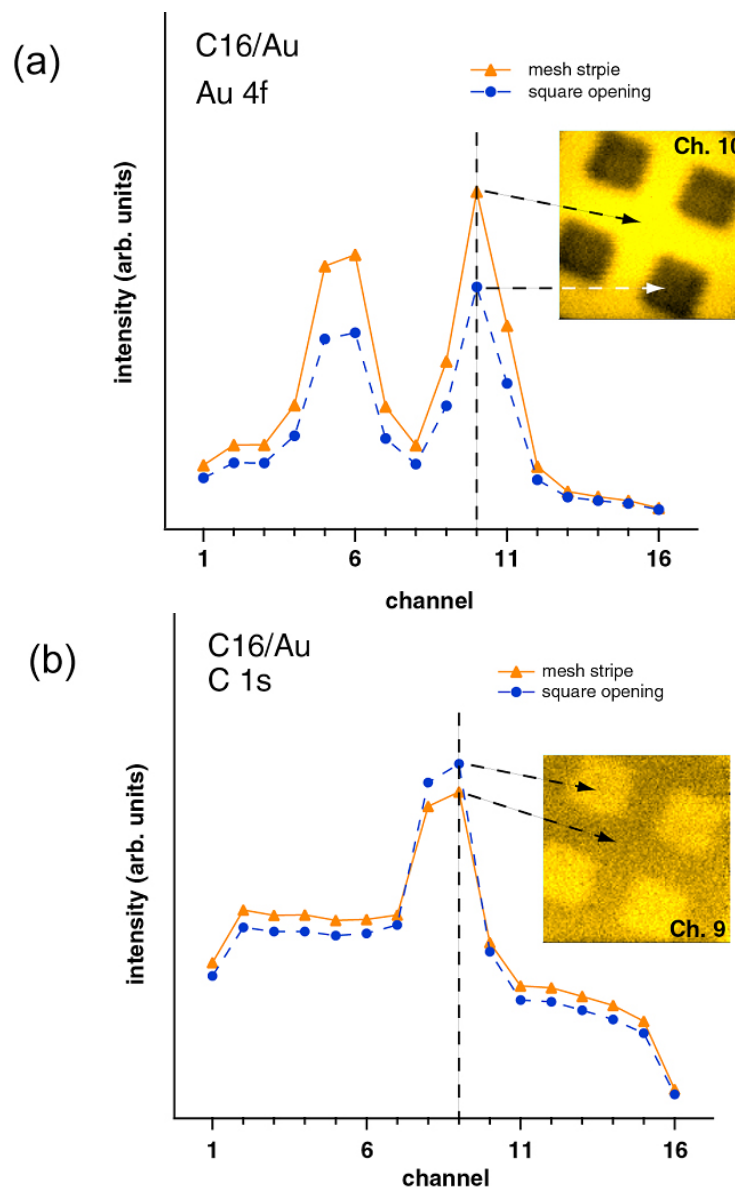


Figure 8. SPEM images and 16-channel small spot HRXPS spectra of electron-beam patterned C16/Au taken at a photon energy of 388 eV. (a) Au 4f spectra derived from the mesh stripe (triangles) and square opening (solid circles) of the 16-channel SPEM image. The image shown here is the Au 4f_{7/2} image from channel number 10. (b) 16-channel C 1s spectra taken from the same area as the Au 4f spectra along with the C 1s image from channel number 9. The size of both images is 24 $\mu\text{m} \times 24 \mu\text{m}$ (120 pixel \times 120 pixel). A pixel dwell time was 60 ms.

“disagreement” has been explained [126] as the adsorption of airborne carbon-containing molecules on the irradiated areas during the air exposure. An enhanced adsorption affinity of the irradiated areas is related to their roughness and the presence of chemically active sites created by irradiation [109, 142].

Soft X-ray beam patterned SAMs

Another example that can show the power of chemical imaging by SPEM is the chemical modification of SFAT SAMs, which were F10H11/Au and F10H2/Ag. Both films are composed of a hydrocarbon chain anchored to the substrate by the thiolate headgroup, and a fluorocarbon chain forming the SAM-ambient interface [138]. Previous HRXPS studies from the pristine film showed three distinct C 1s emissions corresponding to the CH₂, CF₂, and CF₃ moieties [138, 143]. Upon the irradiation, the emissions related to the fluorocarbon moieties decrease while the intensity of the peak originally assigned to the CH₂ entity increases. The latter was explained by the reduced attenuation of the photoelectrons stemming from the hydrocarbon part and the transformation of CF₂ and CF₃ into C-C and C=C species [137, 144, 145].

Figure 9 shows the C 1s SPEM images of *in situ* X-ray patterned F10H11/Au. The writing of an “S” shape pattern was carried out by scanning areas of rectangular shape with the focused X-ray beam using an irradiation time per pixel of 90 ms and pixel width of 500 nm. The photon energy was set at 387 eV. The imaging was performed by scanning a 70 μm × 70 μm area with a dwell time of 60 ms and a pixel width of 700 nm. The images were taken from channels 6 and 13, corresponding to the CF₂ and CH₂ moieties, respectively. Along with the images, Figure 9 presents the 16-channel spectra from the patterned area (orange triangles), the non-patterned area (blue solid circles),

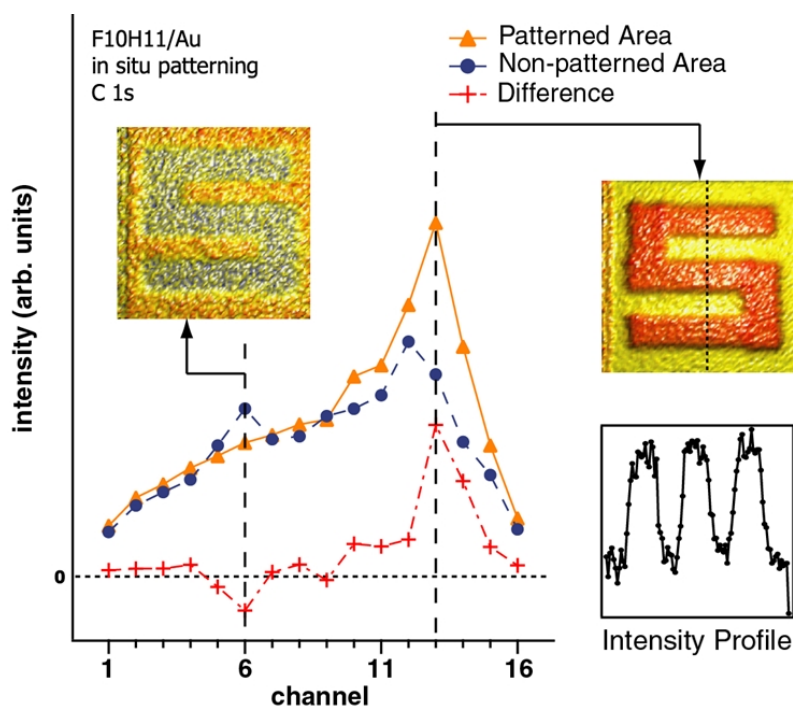


Figure 9. SPEM images (image size 70 μm × 70 μm) and 16-channel HRXPS spectra of a SPEM patterned F10H11/Au taken at a photon energy of 387 eV.

and the spectra difference between the patterned area and non-patterned area (red crosses). The spectra were obtained by the integration over the selected areas of $10 \text{ pixel} \times 10 \text{ pixel}$. The curve below the image of channel 13 is the intensity profile along the dashed line in the image.

As described above, upon X-ray illumination, fluorocarbon species were transformed into C-C and C=C moieties; the contrast inversion of the CF_2 and CH_2 images visualizes this effect. The peak related to the fluorocarbon chain (channel 6) becomes noticeably weaker while the hydrocarbon-related emission (channel 13) shows a strong enhancement in the intensity after the irradiation. This observation is also confirmed by the spectra difference.

Another example of X-ray microbeam patterning is F10H2 on Ag. The writing was carried out by scanning rectangles with same width ($10 \mu\text{m}$), but different lengths varying in steps of $5 \mu\text{m}$. Due to the common origin of the rectangles, this resulted in an exposure time gradient ranging from 30 ms to 180 ms along the stripe [146], as illustrated in the right of Figure 10. The pixel size for the writing was kept at 200 nm. The purpose of this gradient pattern was to study the soft X-ray exposure effect on the SFAT film. The imaging of the gradient pattern was performed with 400 nm pixel and 30 ms of dwell time.

Figure 10 shows the C 1s 16-channel spectra taken from the different areas of the F10H2/Ag gradient pattern, along with the images corresponding to channel 13 (CH_2) and 6 (CF_2). The exposure time was increased from the top to

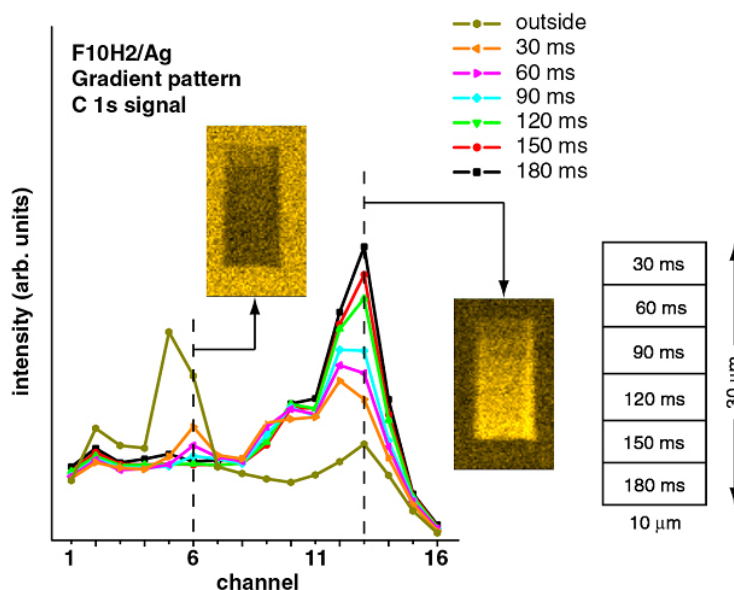


Figure 10. 16-channel C 1s spectra taken from areas inside and outside of a microbeam-patterned F10H2/Ag sample. The exposure time along the written gradient stripe was varied from 30 to 180 ms, the size of the stripe is $10 \mu\text{m} \times 30 \mu\text{m}$, as shown on the right. The SPEM images correspond to CH_2 (channel 13) and CF_2 (channel 6) moieties.

bottom of the stripe. The brightness in the image corresponds to a higher C 1s photoelectron yield. The spectra are the intensity summation over 18 pixel \times 10 pixel rectangles selected along the stripe, to monitor the effect of different exposure times. The spectra show that the fluorocarbon moieties (the peaks at lower channel numbers, i. e., higher binding energies) were gradually transferred to C-F species and different nonsaturated hydrocarbons (the peaks at higher channel numbers) with increasing exposure time. The first 30 ms of exposure results in a sudden intensity drop of the CF₂ peak, which becomes more gradual at further exposure. The inverse contrasts of the “CF₂” and “CH₂” images and the gradual intensity increment of the signal related to hydrocarbons (or decrement of the signal associated with fluorocarbons) suggests that a gradual chemical modification of fluorocarbons to hydrocarbons can be achieved through a precise control of X-ray exposure time.

The above examples show the strength of SPEM for X-ray lithography and subsequent analysis of the prepared structures. The major advantages of this technique lay in its high flexibility, visualization of different chemical state, and the possibility of *in situ* characterization of the fabricated patterns. Particularly, chemical patterns can be produced and studied. Also, gradient patterns can be fabricated, chemically modified (by exposure to suitable molecules inside the SPEM system), and characterized within a single experiment. Although it can be difficult to image weak signals related to small functional groups or buried head groups, and modification of the film is still going on during the imaging process, the above examples showed that SPEM can still provide a unique information that other techniques are difficult to offer.

Imaging and characterization of SAM-based lithographic patterns by PEEM

Along with the SPEM approach, SAM based lithographic patterns can be imaged and characterized by an X-ray PEEM [130]. Since most of the PEEM facilities do not possess an energy filter, the method of choice is usually the tuning of the photon energy, i. e., X-ray absorption microscopy (XAM) in a total electron yield (TEY) mode. As an example, we show in Figure 11 a $\pi^*(\text{NO}_2)$ XAM image of a chemical lithographic pattern obtained by the transformation of the nitro tail group of a 4-nitro-1,1'-biphenyl-4-thiol (NBPT: $\text{NO}_2\text{-(C}_6\text{H}_4)_2\text{-SH}$) SAM into amino ($\text{NH}_2\text{-}$) group (see schema) [133], along with the respective N K-edge X-ray absorption microspot spectra related to the pristine and irradiated areas of the pattern and an intensity profile taken through a similar lithographic pattern. Both image and spectra have been acquired by the PEEM2 [20] at the microscopy branch (7.3.1.1) of the beamline 7.3.1 at the ALS. The pattern in Figure 11(a) has been fabricated by irradiation of NBPT SAM through a mask - carbon QUANTIFOIL membrane

with $1.2\ \mu\text{m}$ circular hole arrays, arranged in squares (Plano). As seen in Figure 11(a), the pattern could be clearly imaged by XAM. The observed contrast results from an interplay of chemically specific spectromicroscopic contrast and non-specific topographic and work function contrasts. In most cases, the spectromicroscopic contrast is the dominating one, as, e. g., in the presented image. According to the N K-edge microspot spectra (Figure 11(b)), the irradiation-induced transformation of the nitro groups of NPBT to amino ones is accompanied by the disappearance of the respective absorption resonance, which results in a low emission intensity as soon as the photon energy will be tuned to its position. In fact, the irradiated areas (dots) of the NPBT-based lithographic pattern deliver a lower TEY signal than the pristine areas. Note that the microspot spectra derived from different areas of the SAM patterns provide specific chemical information. Even at a feature size of about $1\ \mu\text{m}$, the quality of the microspot spectra was comparable with that of the analogous X-ray absorption spectra acquired from homogeneous SAM samples [130].

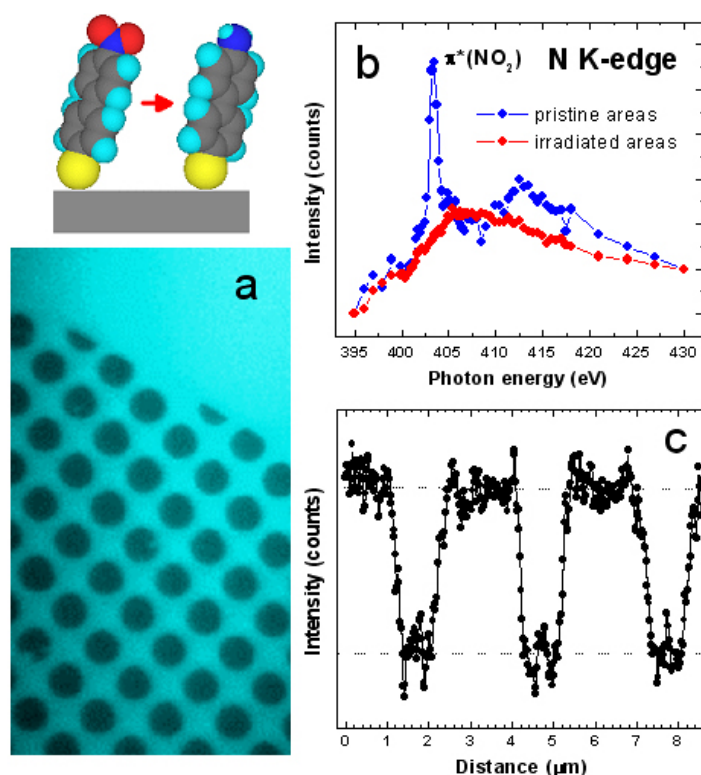


Figure 11. (a) XAM image of a chemical lithographic pattern obtained by the transformation of the nitro tail group of a NPBT SAM into amino group as shown in the schema; the image has been acquired at the position of the π^* resonance of the nitro group (404.0 eV); the diameter of the dots is $1.2\ \mu\text{m}$, (b) normalized N K-edge X-ray absorption microspot spectra related to the pristine and irradiated areas of the pattern, (c) intensity profile taken through the irradiated dots ($1\ \mu\text{m}$) of a similar lithographic pattern.

The lateral resolution of SAM based lithographic patterns as well as the pattern shown in Figure 11(a), in particular, was estimated to be better than 150 nm, which allowed to distinguish the fine structure of 1 μm features. This is demonstrated in Figure 11(c), where an intensity profile taken through a NBPT-based chemical lithographic pattern (similar to the pattern shown in Figure 11(a)) is presented. This intensity profile shows that the illumination of the SAMs within the dot-like openings (1 μm) of the membrane was inhomogeneous during the patterning - there is a systematic intensity rise in the dot centers. Considering that the initial electron flux was homogeneous, it could be only a lens-like effect of these openings, which resulted in a focusing of electrons in their centers.

Carbon nanotubes

SPEM and PEEM have also been successfully employed for the study of carbon nanotubes. This will be discussed in the following. Since their discovery [147], carbon nanotubes (CNTs) have attracted much attention because of their unique structural, electrical, and mechanical properties, such as their highly one-dimensional structure, low threshold voltage for electron field emission, ballistic electron transport, and high mechanical strength [148]. CNTs can be classified into two types, that are multi-walled carbon nanotubes (MWNTs) and single-walled ones (SWNTs). MWNTs consist of coaxial assemblies of several graphene cylinders with diameters in the range of 2-30 nm, separated by the c-plane spacing (approximately 0.34 nm) of graphite. From the application point of view, MWNTs are promising materials as field emitters for flat panel displays. Aligned carbon nanotubes as field emitters are a major advance in this field. Thus, the investigation of the electronic properties of the nanotube tip region is becoming more important. SPEM, a powerful tool to investigate electronic structures, can be utilized to study aligned MWNTs along the nanotube axes with high spatial resolution in order to clarify the local electronic properties directly at the tip region.

In contrast, SWNTs consist of a single graphene sheet rolled into a cylinder with diameters in the range of 1-2 nm exhibiting either metallic or semiconducting behavior depending on their chirality. Several research groups have succeeded in growing suspended SWNT networks on Si and SiO₂ pillars using the chemical vapor deposition (CVD) method assisted by catalyst precursor materials [149, 150]. The electrical properties of the suspended SWNTs are the most important issue in their applications such as self-assembled nano-networks of interconnected nanoelectronic devices. One of the most powerful analytical tools for directly studying the electrical properties of such suspended SWNTs is imaging photoemission microscopy, even though

there remains the issue that the diameters of SWNTs and SWNT bundles are one order of magnitude smaller than the lateral resolution of the microscope.

In the following, the results on the electrical properties of such carbon nanotubes will be shown by means of two types of synchrotron radiation photoemission spectromicroscopes. First, the spatially resolved electronic structure of aligned MWNTs along the tube axes has been analyzed by SPEM at ELETTRA. It has been found that the tips have a larger density of states near the Fermi level than the sidewalls. Next, suspended SWNTs grown on a patterned Si substrate have been studied by means of the SPELEEM system at ELETTRA. The individual suspended SWNTs and/or SWNT bundles have been successfully observed with bright contrast, and work function differences between the SWNTs have been clarified.

Electron density of states of multi-walled carbon nanotube tips

As described in detail in the previous section, a SPEM system consists of a photon focusing system (a combination of a Fresnel zone plate lens and an order sorting aperture), specimen positioning and scanning system, and a hemispherical capacitor analyzer with a 16-channel detector. For the ELETTRA-SPEM, the angle between the incident light (normal to the sample) and the electron energy analyzer is 70° . The MWNTs aligned perpendicularly on a Si substrate were grown using microwave plasma-enhanced chemical vapor deposition with Co as a catalyst. The diameter and the length of the nanotubes were about 30 nm and 10 μm , respectively. The catalytic Co particles are encapsulated at the bottom of the nanotubes [151]. A typical cross-sectional scanning electron microscope (SEM) image of a cleaved sample is shown in Fig. 12(a). The sample was cleaved in air and then annealed at about 200°C for 12 h in the SPEM preparation chamber in order to remove physisorbed molecules. Before annealing, several atomic percent of oxygen were detected by core-level X-ray photoemission spectroscopy (XPS). The oxygen is due to physisorbed molecules and can easily be removed by annealing. After annealing, no other elements than carbon are detected by XPS. The sample was then transferred into the SPEM analysis chamber where the cross-sectional measurements were carried out at room temperature [152]. The lateral resolution, energy resolution, and photon energy are 90 nm, about 0.3 eV, and 497.0 eV, respectively. Figure 12(b) shows a cross-sectional image of the cleaved sample obtained by collecting the C 1s photoelectrons. Figure 13 shows a higher magnification C 1s image. Prominent MWNT bundles are clearly observed, and are found to split into three branches near the tip, indicating that precise focusing was achieved. Figure 14(a) shows the C 1s image of another cross-sectional position. The contrast is dominated by cross-sectional surface topography. The grazing acceptance angle of the analyzer enhances the topographic effects. Brighter parts are seen around the tips and

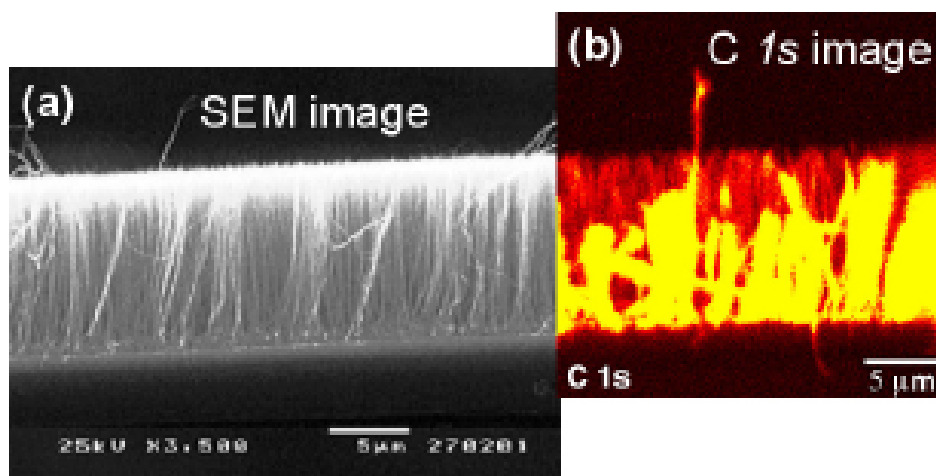


Figure 12. (a) Cross-sectional SEM image of the aligned MWNTs. (b) Cross-sectional SPEM image of the cleaved sample obtained by collecting the C 1s photoelectrons.

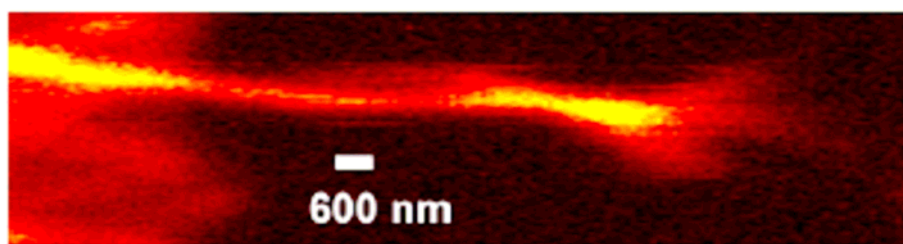


Figure 13. Higher magnification C 1s SPEM image. MWNT bundles split into three branches near the tip.

also in some middle parts with disordered nanotubes, where the disorder is probably caused by cleavage. On the other hand, some middle parts appear very dark due to a shadowing effect by neighboring nanotubes. Figure 14(b) shows a photoelectron intensity profile measured along the line shown in Fig. 14(a). Photoelectron intensity peaks having widths of several hundred nanometers can be clearly observed, corresponding to the diameter of bundles of MWNTs. The valence-band spectra in Fig. 15(a) were measured in spots along the nanotube axes as indicated in Fig. 15(b). Although the overall valence-band spectra from the tips and sidewalls are very similar, a distinct difference is observed in the vicinity of the Fermi level. Spectra 1 and 7 were obtained from tip regions and all others from sidewall regions, including the bright and dark parts, as denoted in the image in Fig. 15(b). The spectra from the sidewall positions are reasonably similar to each other. However, the two tip positions show a substantially larger spectral intensity in the energy range down to approximately 1 eV below the Fermi edge. This is clear evidence that the MWNT tips possess a larger density of states in the vicinity of the Fermi

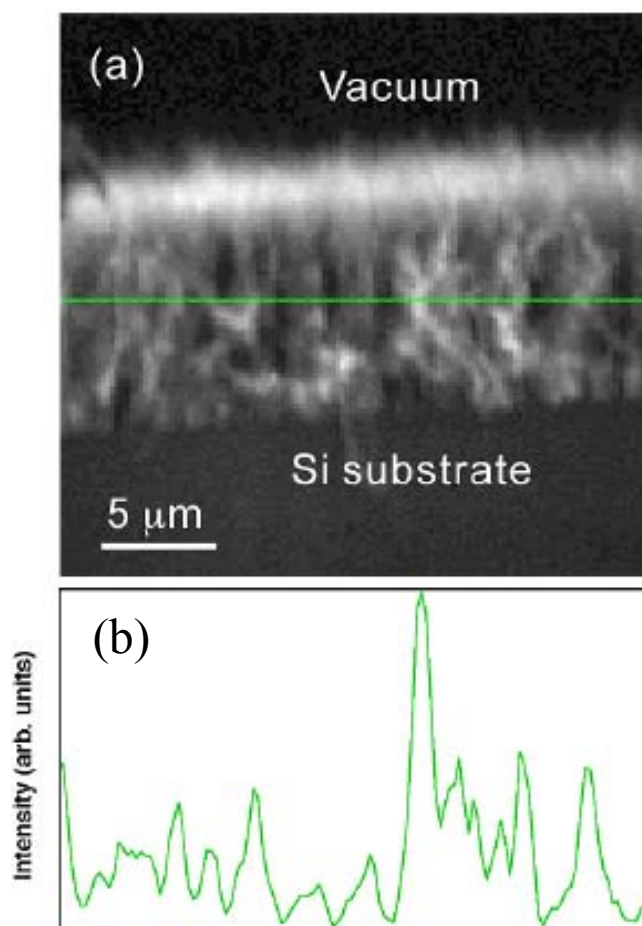


Figure 14. (a) Cross-sectional C 1s SPEM image of the aligned MWNTs, and (b) C 1s photoelectron intensity profile along the line in (a).

level than the sidewalls. Figure 15(c) shows the C 1s spectra of tips and sidewalls. There is a reproducible slight shift of the C 1s spectra from the tips to a lower binding energy by about 50 meV. This slight shift might be due to band bending near the tips, implying that the Fermi level is located inside the valence band at the tips. This will slightly increase the density of states at the Fermi level at the tips. However, the large spectral difference between the tips and sidewalls shown in Fig. 15(a) cannot be explained by a Fermi level shift of only 50 meV at all. Thus, the tips are thought to have a characteristic enhancement in the density of states near the Fermi level, which is not caused by band bending. The results can be interpreted assuming a higher density of dangling bonds at the tips, consistent with the defective nature of the MWNTs. Indeed, our previous TEM study has revealed that most of the graphene sheets in deintercalated MWNTs had a continuous length of only around 10 nm [153]. At the present time, details of the defect formation mechanism are not yet clear.

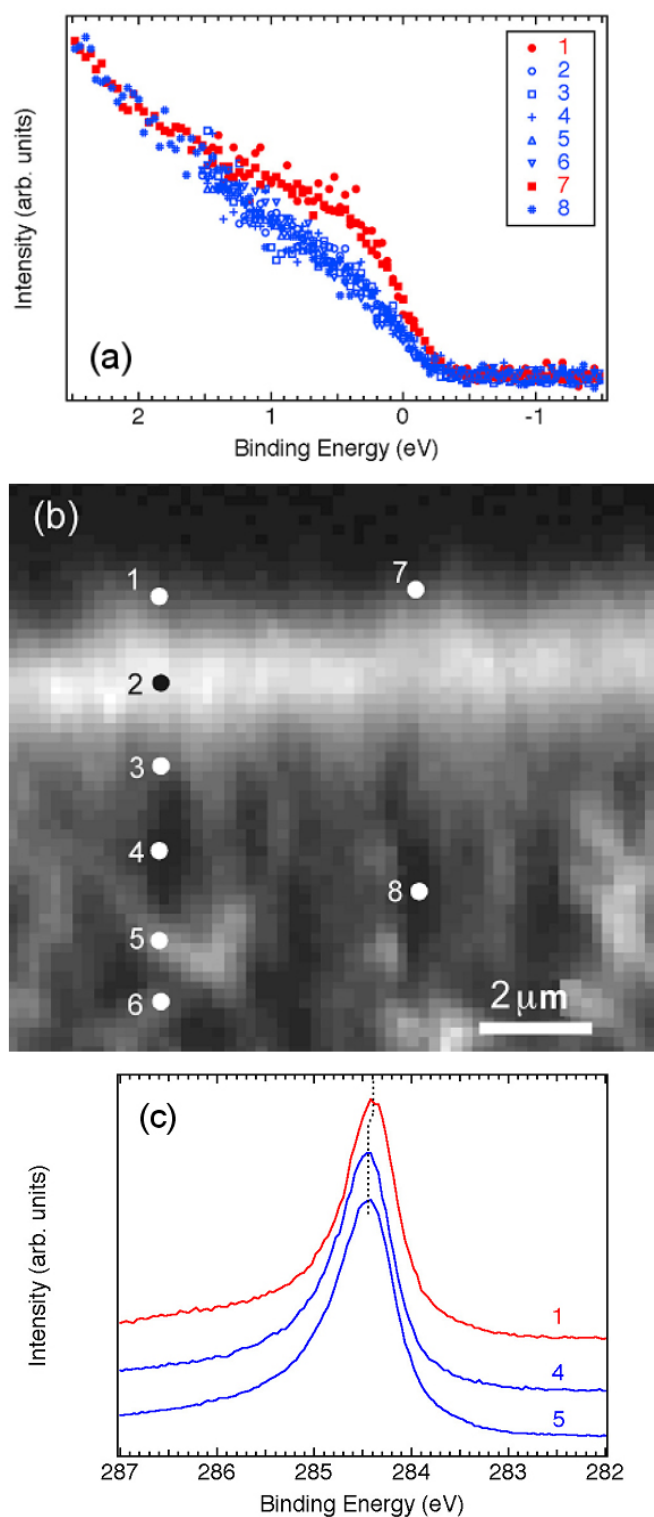


Figure 15. (a) Valence-band photoemission spectra in the vicinity of the Fermi level from spatially selected regions. The positions of the measurements are shown in the C 1s SPEM image in (b). (c) C 1s photoemission spectra from spatially selected regions. The numbers correspond to the measurement positions indicated in (b).

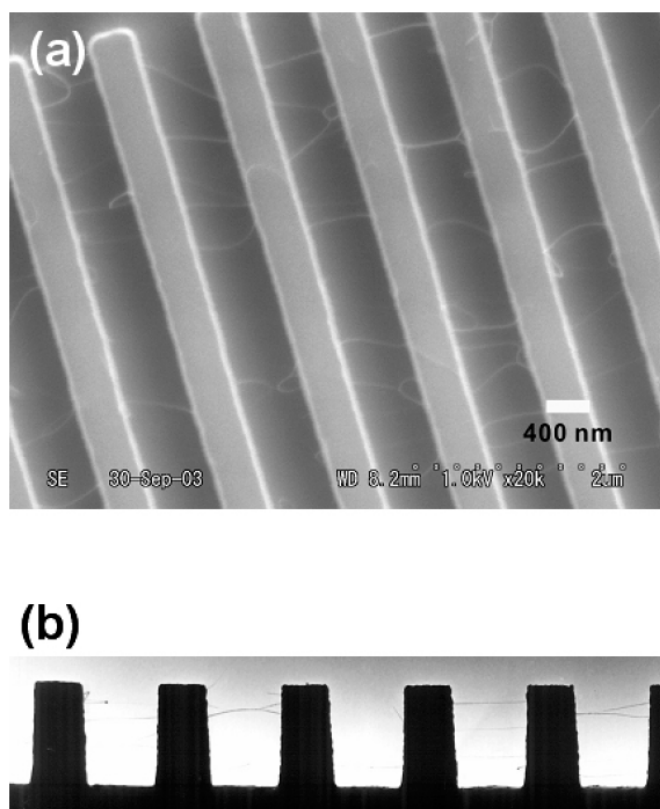


Figure 16. (a) SEM and (b) cross-sectional TEM images of the suspended SWNTs grown on a patterned Si sample.

Work functions of single-walled carbon nanotubes

The work functions of individual SWNTs suspended between patterns on a Si substrate was measured by means of the SPELEEM system, which has a lateral resolution of around 30 nm [59]. This technique is a direct way to evaluate the local work function. Line and space patterns were fabricated on a Si substrate using synchrotron radiation lithography. Line width and height were 400 and 500 nm, respectively. The pattern period was chosen to be 1 μm . SWNTs were grown on the patterned Si using CVD at 900°C and Fe nanoparticles as catalysts [150]. Typical SEM and TEM images of the sample are shown in Fig. 16. Spectromicroscopic experiments were carried out at room temperature after annealing the sample at around 650°C under ultra-high vacuum conditions in the preparation chamber of the SPELEEM. The synchrotron photon energy used here was 350 eV. The synchrotron light illuminates the sample at a grazing incidence angle of 16° from the sample surface. Figure 17 shows typical C 1s images. The individual suspended SWNTs and/or SWNT bundles between the line patterns are successfully observed with bright contrast owing to the shade of the line patterns under the grazing incidence illumination condition of synchrotron light. Secondary electron

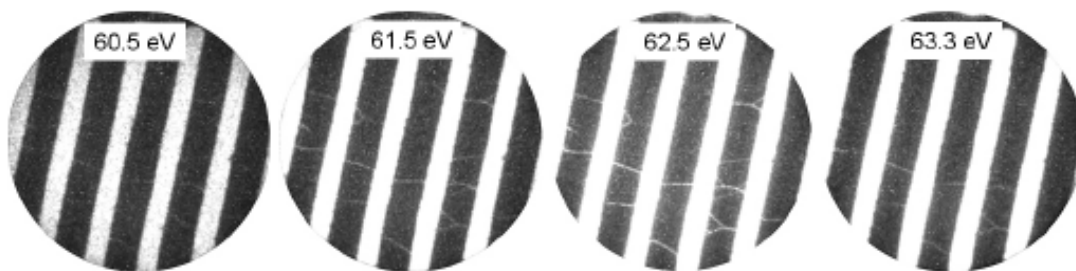


Figure 17. C 1s PEEM images of suspended SWNTs grown on a patterned Si sample. The individual suspended SWNTs and/or SWNT bundles between the line patterns are observed in each image. The energy values as indicated in the figure are kinetic energies. Field of view is $5 \mu\text{m}$.

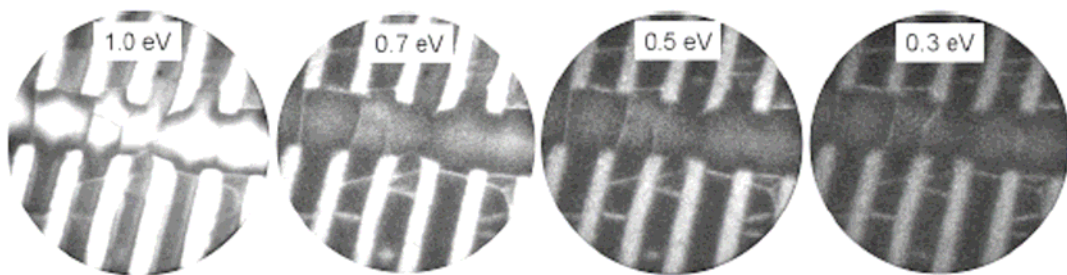


Figure 18. Secondary electron PEEM images of a different sample position as shown in Fig. 17. The energy values as indicated in the figure are kinetic energies. Field of view is $5 \mu\text{m}$.

PEEM images are shown in Fig. 18. The kinetic energy of the secondary electron threshold depends on the local work function, which means that SWNTs having lower work functions can be observed at lower kinetic energies. As shown in Fig. 18, work function differences between the respective SWNTs were clearly observed. The work functions of more than 90 SWNTs were analyzed. The work functions are distributed within an energy range of 0.6 eV with a single peak at the center of the range. A splitting distribution into two groups, suggesting a large work function difference between metallic and semiconducting tubes, was not observed. Furthermore, the results also showed that nearly 90% of the work functions are distributed within an energy range of 0.2 eV. These two specific application examples mentioned above show the effectiveness of both the SPEM and SPELEEM for analyzing the local electronic properties of carbon nanotubes. The results of the spatially resolved electronic structure of aligned MWNTs along the tube axes by SPEM showed that the tips have a larger density of states near the Fermi level than the sidewalls. Even though the diameters of SWNTs and SWNT bundles are one order of magnitude smaller than the lateral resolution

of SPELEEM, the isolated SWNTs and/or SWNT bundles suspended between patterns on the Si substrate were successfully observed as bright contrast.

Conclusions

The complexity of today's advanced materials and specific chemical and electronic properties related to their reduced dimensions have boosted new developments in the field of microscopy. Photoemission microscopies are taking advantage of the well-established method of photoelectron spectroscopy for material analysis and characterization. The two different microscopic tools, viz., PEEM and SPEM offer complimentary capabilities. SPEM has high surface sensitivity and energy resolution, providing direct information on chemical and electronic state, but the acquisition of images or microspot spectra is often accompanied by a partial radiation damage of the sample. PEEM, on the other hand, has comparable or better spatial resolution than SPEM and is capable of fast imaging using various image contrast mechanisms. The community of PEEM users is wide spread largely due to the availability of highly sophisticated commercial systems, which is the driving force for rapid improvements of this technique. It is expected that the ultimate spatial resolution for PEEM will clearly reach a few nm. In comparison, SPEM has a much smaller user group with only a handful of home-made systems available worldwide. However, with the improved fabrication of high-resolution focusing optics, a spatial resolution of SPEM below 50 nm can certainly be achieved. Both microscopes have been proven to be powerful tools for surface and materials science probing the sub-micron regime. Their future depends on their impact on the field of nanoscience and nanotechnology. The selected examples in this article are new approaches. Self-assembled monolayers can provide a basis for the fabrication of different chemical patterns. Complex changes in those monomolecular films, occurring due to the patterning process and subsequent chemical reactions, can be imaged and analyzed by photoemission microscopy. Furthermore, such a drawback as the radiation damage by the focused X-ray beam of SPEM can be transformed into an advantage and utilized for the SAM patterning. The *in situ* patterning and characterization is certainly a novel and promising application of SPEM. Carbon nanotubes as well as any other type of nanowires and nanorods have very distinct electronic properties, which leads to their technological importance. Although the diameters of the tubes are beyond the present resolution capability of the photoemission microscopes, the particular setup of the experiment by taking cross-sectional images of aligned CNTs or measuring suspended CNTs on patterned substrates allows a clear distinction of the local electronic structure. Both examples showed that the combination of SPEM and PEEM is a perfect match in characterizing advanced nano-structured materials.

Acknowledgments

One of the authors (CHC) thanks Mr. S.-C. Wang and Mr. P.-Y. Lin for their skillful help during the SR beamtime; SH and YW would like to thank Dr. S. Suzuki, Dr. L. Gregoratti, Dr. A. Barinov, Dr. B. Kaulich, and Dr. A. Locatelli for their work during the SR beamtime experiments at ELETTRA in Trieste, Italy. MZ acknowledges the help and support by A. Shaporenko, M. Grunze, and J.-D. Liao, and thanks A. Terfort for the synthesis of the SFAT compounds. The self-assembled monolayer project was partially supported by the National Science Council, Taiwan, under grant number: NSC-95-2112-M-213-013, DFG (ZH 63/9-2), and a NSC/DAAD grant 423/rc-PPP-sr, and U.S. DEO contract DE-AC03-76SF00. Work done by both SPEM and SPELEEM at ELETTRA was partly supported by Special Coordination Funds of the Science and Technology Agency of the Japanese Government.

References

1. S. Hüfner, S. Schmidt, and F. Reinert, *Nucl. Instr. and Meth. A* **547**, 8 (2005).
2. F. Adams, L. Van Vaeck, and R. Barrett, *Spectrochimica Acta Part B* **60**, 13 (2005).
3. M. Kiskinova, M. Marsi, E. Di Fabrizio, and M. Gentili, *Surf. Rev. Lett.* **6**, 265 (1999).
4. T. Warwick, H. Ade, S. Cerasari, J. Denlinger, K. Franck, A. Garcia, S. Hayakawa, A. Hitchcock, J. Kikuma, S. Klingler, et al., *J. Synchrotron Rad.* **5**, 1090 (1998).
5. L. Casalis, L. Gregoratti, M. Kiskinova, G. Margaritondo, F. M. Braz Fernandes, R. J. Silva, G. R. Morrison, and A. W. Potts, *Surf. Interface Anal.* **25**, 374 (1997).
6. F. Barbo, M. Bertolo, A. Bianco, G. Cautero, S. Fontana, T. K. Johal, S. La Rosa, G. Margaritondo, and K. Kaznacheyev, *Rev. Sci. Instrum.* **71**, 5 (2000).
7. R. Klauser, I.-H. Hong, T.-H. Lee, G.-C. Yin, D.-H. Wei, K.-L. Tsang, T. J. Chuang, S.-C. Wang, S. Gwo, M. Zharnikov, et al., *Surf. Rev. Lett.* **9**, 213 (2002).
8. I.-H. Hong, T.-H. Lee, G.-C. Yin, D.-H. Wei, J.-M. Juang, T.-E. Dann, R. Klauser, T. J. Chuang, C.-T. Chen, and K.-L. Tsang, *Nucl. Instr. Meth. A* **467-468**, 905 (2001).
9. C.-H. Ko, R. Klauser, D.-H. Wei, H.-H. Chan, and T. J. Chuang, *J. Synchrotron Rad.* **5**, 299 (1998).
10. U. Johansson, R. Nyholm, C. Törnevik, and A. Flodström, *Rev. Sci. Instrum.* **66**, 1398 (1995).
11. TH. Schmidt, U. Groh, R. Fink, E. Umbach, O. Schaff, W. Engel, B. Richter, H. Kühlenbeck, R. Schlögl, H.-J. Freund, A. M. Bradshaw, D. Preikszas, P. Hartel, R. Spehr, H. Rose, G. Lilienkamp, E. Bauer, and G. Benner, *Surf. Rev. Lett.* **9**, 223 (2002).
12. H.-J. Shin and M. Lee, *Nucl. Instr. Meth. A* **467-468**, 909 (2001).
13. G. Margaritondo and F. Cerrina, *Nucl. Instrum. Methods Phys. Res. A* **291**, 26 (1990).
14. B. P. Tonner and G. R. Harp, *Rev. Sci. Instrum.* **59**, 853 (1988).
15. H. H. Rotermund, W. Engel, M. Kordesch, and G. Ertl, *Nature* **343**, 355 (1990).

16. E. Bauer, Rep. Prog. Phys. **57**, 895 (1994).
17. T. Schmidt, S. Heun, J. Slezak, J. Diaz, K. C. Prince, G. Lilienkamp, and E. Bauer, Surf. Rev. Lett. **5**, 1287 (1998).
18. R. M. Tromp, M. Mankos, M. C. Reuter, A. W. Ellis, and M. Copel, Surf. Rev. Lett. **5**, 1189 (1998).
19. J. Stöhr, H. A. Padmore, S. Anders, T. Stammler, and M. R. Scheinfein, Surf. Rev. Lett. **5**, 1297 (1998).
20. S. Anders, H. A. Padmore, R. M. Duarte, T. Renner, T. Stammler, A. Scholl, M. R. Scheinfein, J. Stöhr, L. Séve, and B. Sinkovic, Rev. Sci. Instrum. **70**, 3973 (1999).
21. B. L. Henke, J. A. Smith, and D. T. Attwood, J. Appl. Phys. **48**, 1852 (1977).
22. G. F. Rempfer, W. P. Skoczylas, and O. H. Griffith, Ultramicroscopy **36**, 196 (1991).
23. B. H. Frazer, M. Girasole, L. M. Wiese, T. Franz, and G. De Stasio, Ultramicroscopy **99**, 87 (2004).
24. W. Engel, M. E. Kordesch, H. H. Rotermund, S. Kubala, and A. von Oertzen, Ultramicroscopy **36**, 148 (1991).
25. H. Yasufuku, H. Yoshikawa, M. Kimura, K. Ito, K. Tani, and S. Fukushima, Surf. Interface Anal. **36**, 892 (2004).
26. T. Wakita, T. Taniuchi, K. Ono, M. Suzuki, N. Kawamura, M. Takagaki, H. Miyagawa, F. Guo, T. Nakamura, T. Muro, et al., Jpn. J. Appl. Phys. **45**, 1886 (2006).
27. F. Polack and S. Lowenthal, Rev. Sci. Instrum. **52**, 207 (1981).
28. R. N. Watts, S. Liang, Z. H. Levine, T. B. Lucatorto, F. Polack, and M. R. Scheinfein, Rev. Sci. Instrum. **68**, 3464 (1997).
29. G. De Stasio and G. Margaritondo, J. Electron Spectrosc. Relat. Phenom. **84**, 137 (1997).
30. Y. Hwu, W. L. Tsai, B. Lai, J. H. Je, G. H. Fecher, M. Bertolo, and G. Margaritondo, Surf. Sci. **480**, 188 (2001).
31. L. A. Bakaleynikov, E. Y. Flegontova, and E. Zolotoyabko, J. Electron Spectrosc. Relat. Phenom. **151**, 97 (2006).
32. W. Gudat and C. Kunz, Phys. Rev. Lett. **29**, 169 (1972).
33. S. Anders, H. A. Padmore, A. Scholl, M. R. Scheinfein, J. Stöhr, and J. Lüning, Synchrotron Radiation News **12** (3), 17 (1999).
34. E. Bauer, Ultramicroscopy **36**, 52 (1991).
35. W. Swiech, G. H. Fecher, C. Ziethen, O. Schmidt, G. Schönhense, K. Grzelakowski, C. M. Schneider, R. Frömter, H. P. Oepen, and J. Kirschner, J. Electron Spectrosc. Relat. Phenom. **84**, 171 (1997).
36. Staib Instruments (www.staibinstruments.com).
37. P. Hoffmann, R. P. Mikalo, and D. Schmeißer, Solid-State Electronics **44**, 837 (2000).
38. M. Merkel, M. Escher, J. Settemeyer, D. Funnemann, A. Oelsner, C. Ziethen, O. Schmidt, M. Klais, and G. Schönhense, Surf. Sci. **480**, 196 (2001).
39. A. Oelsner, O. Schmidt, M. Schicketanz, M. Klais, G. Schönhense, V. Mergel, O. Jagutzki, and H. Schmidt-Böcking, Rev. Sci. Instrum. **72**, 3968 (2001).
40. G. Schönhense, A. Oelsner, O. Schmidt, G. H. Fecher, V. Mergel, O. Jagutzki, and H. Schmidt-Böcking, Surf. Sci. **480**, 180 (2001).

41. G. K. L. Marx, V. Gerheim, and G. Schönhense, *J. Electron Spectrosc. Relat. Phenom.* **84**, 251 (1997).
42. Y. Sakai, M. Kato, S. Masuda, Y. Harada, and T. Ichinokawa, *Surf. Rev. Lett.* **5**, 1199 (1998).
43. H. Yasufuku, Y. Ohminami, T. Tsutsumi, H. Niimi, N. Matsudaira, K. Asakura, M. Kato, Y. Sakai, Y. Kitajima, and Y. Iwasawa, *Jpn. J. Appl. Phys.* **43**, 7682 (2004).
44. S. Yamamoto, S. Masuda, H. Yasufuku, N. Ueno, Y. Harada, T. Ichinokawa, M. Kato, and Y. Sakai, *J. Appl. Phys.* **82**, 2954 (1997).
45. R. Wichtendahl, R. Fink, H. Kuhlenbeck, D. Preikszas, H. Rose, R. Spehr, P. Hartel, W. Engel, R. Schlögl, H.-J. Freund, et al., *Surf. Rev. Lett.* **5**, 1249 (1998).
46. L. H. Veneklasen, *Ultramicroscopy* **36**, 76 (1991).
47. B. P. Tonner, D. Dunham, T. Droubay, and M. Pauli, *J. Electron Spectrosc. Relat. Phenom.* **84**, 211 (1997).
48. C. Kim, P. L. King, P. Pianetta, M. A. Kelly, and C. A. Bryson, *Rev. Sci. Instrum.* **64**, 1187 (1993).
49. G. Lilienkamp, EUREM 12, Brno, Czech Republic, July 9-14, p. **I 177** (2000).
50. K. Grzelakowski, *Surf. Sci.* **566-568**, 869 (2004).
51. K. Grzelakowski, *J. Phys.: Condens. Matter* **17**, S1351 (2005).
52. M. Escher, N. Weber, M. Merkel, B. Krömker, D. Funnemann, S. Schmidt, F. Reinert, F. Forster, S. Hüfner, P. Bernhard, et al., *J. Electron Spectrosc. Relat. Phenom.* **144-147**, 1179 (2005).
53. M. Escher, N. Weber, M. Merkel, C. Ziethen, P. Bernhard, G. Schönhense, S. Schmidt, F. Forster, F. Reinert, B. Krömker, and D. Funnemann, *J. Phys.: Condens. Matter* **17**, S1329 (2005).
54. O. Renault, R. Brochier, P.-H. Haumesser, N. Barrett, B. Krömker, and D. Funnemann, e-J. *Surf. Sci. Nanotech.* **4**, 431 (2006).
55. ELMITEC GmbH (www.elmitec.de).
56. L. H. Veneklasen, *Rev. Sci. Instrum.* **63**, 5513 (1992).
57. C. Quitmann, U. Flechsig, L. Patthey, T. Schmidt, G. Ingold, M. Howells, M. Janousch, and R. Abela, *Surf. Sci.* **480**, 173 (2001).
58. F. Guo, T. Wakita, H. Shimizu, T. Matsushita, T. Yasue, T. Koshikawa, E. Bauer, and K. Kobayashi, *J. Phys.: Condens. Matter* **17**, S1363 (2005).
59. S. Heun, T. Schmidt, J. Slezak, J. Diaz, K. C. Prince, B. H. Müller, and A. Franciosi, *Journal of Crystal Growth* **201/202**, 795 (1999).
60. A. Locatelli and S. Heun, to be published.
61. S. Heun, Y. Watanabe, B. Ressel, D. Bottomley, T. Schmidt, and K. C. Prince, *Phys. Rev. B* **63**, 125335 (2001).
62. G. Biasiol, S. Heun, G. B. Golinelli, A. Locatelli, T. O. Montes, F. Z. Guo, C. Hofer, C. Teichert, and L. Sorba, *Appl. Phys. Lett.* **87**, 223106 (2005).
63. F. Ratto, A. Locatelli, S. Fontana, S. Kharrazi, S. Ashtaputre, S. K. Kulkarni, S. Heun, and F. Rosei, *Small* **2**, 401 (2006).
64. W. Kuch, L. I. Chelaru, F. Offi, M. Kotsugi, and J. Kirschner, *J. Vac. Sci. Technol. B* **20**, 2543 (2002).
65. M. Lazzarino, S. Heun, B. Ressel, K. C. Prince, P. Pingue, and C. Ascoli, *Appl. Phys. Lett.* **81**, 2842 (2002).

66. S. Heun, S. Kremmer, D. Ercolani, H. Wurmbauer, and C. Teichert, *J. Appl. Phys.* **97**, 104333 (2005).
67. D. Ercolani, M. Lazzarino, G. Mori, B. Ressel, L. Sorba, Locatelli, S. Cherifi, A. Ballestrazzi, and S. Heun, *Adv. Funct. Mater.* **15**, 587 (2005).
68. L. Aballe, A. Barinov, A. Locatelli, S. Heun, and M. Kiskinova, *Phys. Rev. Lett.* **93**, 196103 (2004).
69. S. Suzuki, Y. Watanabe, Y. Homma, S. Fukuba, S. Heun, and A. Locatelli, *Appl. Phys. Lett.* **85**, 127 (2004).
70. F.-J. Meyer zu Heringdorf, T. Schmidt, S. Heun, R. Hild, P. Zahl, B. Ressel, E. Bauer, and M. Horn-von Hoegen, *Phys. Rev. Lett.* **86**, 5088 (2001).
71. T. Koshikawa, H. Shimizu, R. Amakawa, T. Ikuta, T. Yasue, and E. Bauer, *J. Phys.: Condens. Matter* **17**, S1371 (2005).
72. G. Schönhense and H. Spieker, *J. Vac. Sci. Technol. B* **20**, 2526 (2002).
73. A. Bleloch and A. Lupini, *Materials Today* **7** (12), 42 (2004).
74. C. Hetherington, *Materials Today* **7** (12), 50 (2004).
75. P. D. Nellist, M. F. Chisholm, N. Dellby, O. L. Krivanek, M. Murfitt, Z. S. Szilagyi, A. R. Lupini, A. Borisevich, W. H. Sides, Jr., and S. J. Pennycook, *Science* **305**, 1741 (2004).
76. H. Niimi, T. Tsutsumi, H. Matsudaira, T. Kawasaki, S. Suzuki, W.-J. Chun, M. Kato, Y. Kitajima, Y. Iwasawa, and K. Asakura, *Appl. Surf. Sci.* **237**, 641 (2004).
77. H. Niimi, M. Kato, T. Tsutsumi, T. Kawasaki, H. Matsudaira, S. Suzuki, W.-J. Chun, Y. Kitajima, M. Kudo, and K. Asakura, *Appl. Surf. Sci.* **241**, 131 (2005).
78. G. F. Rempfer, D. M. Desloge, W. P. Skoczylas, and O. H. Griffith, *Microsc. Microanal.* **3**, 14 (1997).
79. R. Fink, M. R. Weiss, E. Umbach, D. Preikszas, H. Rose, R. Spehr, P. Hartel, W. Engel, R. Degenhardt, R. Wichtendahl, et al., *J. Electron Spectrosc. Relat. Phenom.* **84**, 231 (1997).
80. J. Feng, H. Padmore, D. H. Wei, S. Anders, Y. Wu, Scholl, and D. Robin, *Rev. Sci. Instrum.* **73**, 1514 (2002).
81. W. Wan, J. Feng, H. A. Padmore, and D. S. Robin, *Nucl. Instr. Meth. A* **519**, 222 (2004).
82. Y. K. Wu, D. S. Robin, E. Forest, R. Schlueter, S. Anders, J. Feng, H. Padmore, and D. H. Wei, *Nucl. Instr. Meth. A* **519**, 230 (2004).
83. J. Feng, E. Forest, A. A. MacDowell, M. Marcus, H. Padmore, S. Raoux, D. Robin, A. Scholl, R. Schlueter, P. Schmid, et al., *J. Phys.: Condens. Matter* **17**, S1339 (2005).
84. P. Schmid, J. Feng, H. Padmore, D. Robin, H. Rose, R. Schlueter, W. Wan, E. Forest, and Y. Wu, *Rev. Sci. Instrum.* **76**, 023302 (2005).
85. S. Günther, B. Kaulich, L. Gregoratti, and M. Kiskinova, *Prog. Surf. Sci.* **70**, 187 (2002).
86. D. Attwood, *Soft X-rays and Extreme Ultraviolet Radiation: Principles and Applications* (Cambridge University Press, Cambridge, 1999).
87. A. G. Michette, *Optical Systems for Soft X-Rays* (Plenum, London, 1986).
88. W. Yun, B. Lai, Z. Cai, J. Maser, D. Legnini, E. Gluskin, Z. Chen, A. A. Krasnoperova, Y. Vladimirovsky, F. Cerrina, et al., *Rev. Sci. Instrum.* **70**, 2238 (1999).

89. F. Cerrina, *J. Electron Spectrosc. Relat. Phenom.* **76**, 9 (1995).
90. T. Kiyokura, F. Maeda, Y. Watanabe, Y. Kadota, Y. Iketaki, Y. Horikawa, M. Oshima, E. Shigemasa, and A. Yagishita, *J. Vac. Sci. Technol. A* **16**, 1086 (1998).
91. J. Kirz and H. Rarback, *Rev. Sci. Instrum.* **56**, 1 (1985).
92. J. Kirz, *J. Opt. Soc. Amer.* **64**, 301 (1974).
93. H. Ade, J. Kirz, S. L. Hulbert, E. D. Johnson, E. Anderson, and D. Kern, *Appl. Phys. Lett.* **56**, 1841 (1990).
94. A. K. Ray-Chaudhuri, W. Ng, S. Liang, S. Singh, J. T. Welnak, J. P. Wallace, C. Capasso, F. Cerrina, G. Margaritondo, J. H. Underwood, et al., *J. Vac. Sci. Technol.* **A11**, 2324 (1993).
95. H. Ade, A. P. Smith, H. Zhang, G. R. Zhuang, J. Kirz, E. Rightor, and A. Hitchcock, *J. Electron Spectrosc. Relat. Phenom.* **84**, 53 (1997).
96. A. Stampfl, C.-H. Chen, S.-C. Wang, M.-L. Huang, and R. Klauser, *J. Electron Spectrosc. Relat. Phenom.* **144-147**, 417 (2005).
97. S. Günther, A. Kolmakov, J. Kovac, and M. Kiskinova, *Ultramicroscopy* **75**, 35 (1998).
98. W. Chao, B. D. Harteneck, J. A. Liddle, E. H. Anderson, and D. T. Attwood, *Nature* **435**, 1210 (2005).
99. O. Hignette, P. Cloetens, C. Morawe, P. Bernard, and W. Ludwig, in *ESRF Highlights 2005* (ESRF, Grenoble, France, 2006).
100. J. W. Chiou, J. C. Jan, H. M. Tsai, W. F. Pong, M.-H. Tsai, I.-H. Hong, R. Klauser, J. F. Lee, C. W. Hsu, H. M. Lin, et al., *Appl. Phys. Lett.* **82**, 3949 (2003).
101. J. W. Chiou, J. C. Jan, H. M. Tsai, C. W. Bao, W. F. Pong, M.-H. Tsai, I.-H. Hong, R. Klauser, J. F. Lee, J. J. Wu, et al., *Appl. Phys. Lett.* **84**, 3462 (2004).
102. J. W. Chiou, K. P. Krishna Kumar, J. C. Jan, H. M. Tsai, C. W. Bao, W. F. Pong, F. Z. Chien, M.-H. Tsai, I.-H. Hong, R. Klauser, et al., *Appl. Phys. Lett.* **85**, 3220 (2004).
103. J. W. Chiou, H. M. Tsai, C. W. Pao, C. L. Dong, C. L. Chang, F. Z. Chien, W. F. Pong, M.-H. Tsai, S. Shi, C. F. Chen, et al., *J. Phys.: Condens. Matter* **17**, 7523 (2005).
104. M. Tello, R. Garcia, J. A. Martín-Gago, N. F. Martínez, M. S. Martín-Gonzalez, L. Aballe, A. Barinov, and L. Gregoratti, *Adv. Mater.* **17**, 1480 (2005).
105. A. Schaak, S. Günther, F. Esch, E. Schütz, M. Hinz, M. Marsi, M. Kiskinova, and R. Imbihl, *Phys. Rev. Lett.* **83**, 1882 (1999).
106. P. Dudin, A. Barinov, L. Gregoratti, M. Kiskinova, F. Esch, C. Dri, C. Africh, and G. Comelli, *J. Phys. Chem. B* **109**, 13649 (2005).
107. P. Melpignano, A. Baron-Toaldo, V. Biondo, S. Priante, R. Zamboni, M. Murgia, S. Caria, L. Gregoratti, A. Barinov, and M. Kiskinova, *Appl. Phys. Lett.* **86**, 041105 (2005).
108. J.-S. Kang, G. Kim, S. C. Wi, S. S. Lee, S. Choi, S. Cho, S. Han, K. H. Kim, H. J. Song, H. J. Shin, et al., *Phys. Rev. Lett.* **94**, 147202 (2005).
109. M. Zharnikov and M. Grunze, *J. Vac. Sci. Technol. B* **20**, 1793 (2002).
110. J. C. Love, L. A. Estroff, J. K. Kriebel, R. G. Nuzzo, and G. M. Whitesides, *Chem. Rev.* **105**, 1103 (2005).
111. A. Ulman, *Chem. Rev.* **96**, 1533 (1996).
112. R. K. Smith, P. A. Lewis, and P. S. Weiss, *Prog. Surf. Sci.* **75**, 1 (2004).

113. Y.-L. Loo, R. L. Willett, K. W. Baldwin, and J. A. Rogers, *J. Am. Chem. Soc.* **124**, 7654 (2002).
114. T. W. Odom, V. R. Thalladi, J. C. Love, and G. M. Whitesides, *J. Am. Chem. Soc.* **124**, 12112 (2002).
115. R. D. Piner, J. Zhu, F. Xu, S. Hong, and C. A. Mirkin, *Science* **283**, 661 (1999).
116. B. D. Gates, Q. Xu, M. Stewart, D. Ryan, C. G. Willson, and G. M. Whitesides, *Chem. Rev.* **105**, 1171 (2005).
117. S. O. Kim, H. H. Solak, M. P. Stoykovich, N. J. Ferrier, J. J. de Pablo, and P. F. Nealey, *Nature* **424**, 411 (2003).
118. S. Xu and G.-Y. Liu, *Langmuir* **13**, 127 (1997).
119. R. Maoz, E. Frydman, S. R. Cohen, and J. Sagiv, *Adv. Mater.* **12**, 725 (2000).
120. R. R. Fuierer, R. L. Carroll, D. L. Feldheim, and C. B. Gorman, *Adv. Mater.* **14**, 154 (2002).
121. S. Liu, R. Maoz, and J. Sagiv, *Nano Lett.* **4**, 845 (2004).
122. R. García, R. V. Martínez, and J. Martínez, *Chem. Soc. Rev.* **35**, 29 (2006).
123. R. C. Tiberio, H. G. Craighead, M. Lercel, T. Lau, C. W. Sheen, and D. L. Allara, *Appl. Phys. Lett.* **62**, 476 (1993).
124. H. U. Müller, C. David, B. Völkel, and M. Grunze, *J. Vac. Sci. Technol.* **13**, 2846 (1995).
125. A. Götzhäuser, W. Geyer, V. Stadler, W. Eck, M. Grunze, K. Edinger, T. Weimann, and P. Hinze, *J. Vac. Sci. Technol.* **18**, 3414 (2000).
126. R. Klauser, I.-H. Hong, S.-C. Wang, M. Zharnikov, Paul, A. Götzhäuser, A. Terfort, and T. J. Chuang, *J. Phys. Chem. B* **107**, 13133 (2003).
127. R. Klauser, M.-L. Huang, S.-C. Wang, C.-H. Chen, T. J. Chuang, A. Terfort, and M. Zharnikov, *Langmuir* **20**, 2050 (2004).
128. M. P. Kiskinova, *Surf. Interface Anal.* **30**, 464 (2000).
129. M.-H. Hsu, W.-S. Hu, J.-J. Lin, Y.-J. Hsu, D.-H. Wei, C.-W. Yang, C.-S. Chang, and Y.-T. Tao, *Langmuir* **20**, 3641 (2004).
130. M. Zharnikov, A. Shaporenko, A. Paul, A. Götzhäuser, and A. Scholl, *J. Phys. Chem. B* **109**, 5168 (2005).
131. W. S. Hu, Y. T. Tao, Y. J. Hsu, D. H. Wei, and Y. S. Wu, *Langmuir* **21**, 2260 (2005).
132. W. Geyer, V. Stadler, W. Eck, M. Zharnikov, A. Götzhäuser, and M. Grunze, *Appl. Phys. Lett.* **75**, 2401 (1999).
133. W. Eck, V. Stadler, W. Geyer, M. Zharnikov, A. Götzhäuser, and M. Grunze, *Adv. Mater.* **12**, 805 (2000).
134. P. E. Laibinis, R. L. Graham, H. A. Biebuyck, and G. M. Whitesides, *Science* **254**, 981 (1991).
135. K. Heister, M. Zharnikov, M. Grunze, and L. S. O. Johansson, *J. Phys. Chem. B* **105**, 4058 (2001).
136. M. Gaupe, T. Koini, V. Wang, G. M. Nassif, J. R. Colorado, R. J. Villazana, H. Dong, Y. F. Miura, O. E. Shmakova, and T. R. Lee, *J. Fluorine Chem.* **93**, 107 (1998).
137. S. Frey, K. Heister, M. Zharnikov, and M. Grunze, *Phys. Chem. Chem. Phys.* **2**, 1979 (2000).

138. S. Frey, K. Heister, M. Zharnikov, M. Grunze, K. Tamada, J. R. Colorado, M. Graupe, O. E. Shmakova, and T. R. Lee, *Isr. J. Chem.* **40**, 81 (2000).
139. J. F. Kang, A. Ulman, S. Liao, R. Jordan, G. Yang, and G.-Y. Liu, *Langmuir* **17**, 95 (2001).
140. M. Zharnikov, W. Geyer, A. Götzhäuser, S. Frey, and M. Grunze, *Phys. Chem. Chem. Phys.* **1**, 3163 (1999).
141. M. Zharnikov, S. Frey, K. Heister, and M. Grunze, *Langmuir* **16**, 2697 (2000).
142. H. U. Müller, M. Zharnikov, B. Völkel, A. Schertel, P. Harder, and M. Grunze, *J. Phys. Chem. B* **102**, 7949 (1998).
143. M. Zharnikov and M. Grunze, *J. Phys.: Condens. Matter* **13**, 11333 (2001).
144. A. J. Wagner, K. Han, A. L. Vaught, and D. H. Fairbrother, *J. Phys. Chem. B* **104**, 3291 (2000).
145. C. C. Perry, A. J. Wagner, and D. H. Fairbrother, *Chem. Phys.* **280**, 111 (2002).
146. R. Klausner, C.-H. Chen, M.-L. Huang, S.-C. Wang, T. J. Chuang, and M. Zharnikov, *J. Electron Spectrosc. Relat. Phenom.* **144-147**, 393 (2005).
147. S. Iijima, *Nature* **354**, 56 (1991).
148. M. S. Dresselhaus, G. Dresselhaus, and P. C. Eklund, *Science of Fullerenes and Carbon Nanotubes* (Academic Press, San Diego, CA, 1996).
149. N. R. Franklin and H. Dai, *Adv. Mater.* **12**, 890 (2000).
150. Y. Homma, Y. Kobayashi, T. Ogino, and T. Yamashita, *Appl. Phys. Lett.* **81**, 2261 (2002).
151. C. Bower, O. Zhou, W. Zhu, D. J. Werder, and S. Jin, *Appl. Phys. Lett.* **77**, 2767 (2000).
152. S. Suzuki, Y. Watanabe, T. Ogino, S. Heun, L. Gregoratti, Barinov, B. Kaulich, M. Kiskinova, W. Zhu, Bower, et al., *Phys. Rev. B* **66**, 035414 (2002).
153. O. Zhou, R. M. Fleming, D. W. Murphy, C. H. Chen, R. C. Haddon, A. P. Ramirez, and S. H. Glarum, *Science* **263**, 1744 (1994).